Received: 19 May 2019 | Revised: 28 December 2019 | Accepted: 8 January 2020
DOI: 10.1002/fld.4808

RESEARCH ARTICLE

WILEY

Finite element computations of viscoelastic two-phase flows using local projection stabilization

Jagannath Venkatesan | **Sashikumaar Ganesan**

Computational Mathematics Group, Department of Computational and Data Sciences, Indian Institute of Science, Bangalore, India

Correspondence
Jagannath Venkatesan, Computational Mathematics Group, Department of Computational and Data Sciences, Indian Institute of Science, Bangalore, India.
Email: jagannathv@iisc.ac.in

Summary

A three-field local projection stabilized (LPS) finite element method is developed for computations of a three-dimensional axisymmetric buoyancy driven liquid drop rising in a liquid column where one of the liquid is viscoelastic. The two-phase flow is described by the time-dependent incompressible Navier-Stokes equations, whereas the viscoelasticity is modeled by the Giesekus constitutive equation in a time-dependent domain. The arbitrary Lagrangian-Eulerian (ALE) formulation with finite elements is used to solve the governing equations in the time-dependent domain. Interface-resolved moving meshes in ALE allows to incorporate the interfacial tension force and jumps in the material parameters accurately. A one-level LPS based on an enriched approximation space and a discontinuous projection space is used to stabilize the numerical scheme. A comprehensive numerical investigation is performed for a Newtonian drop rising in a viscoelastic fluid column and a viscoelastic drop rising in a Newtonian fluid column. The influence of the viscosity ratio, Newtonian solvent ratio, Giesekus mobility factor, and the Eötvös number on the drop dynamics are analyzed. The numerical study shows that beyond a critical Capillary number, a Newtonian drop rising in a viscoelastic fluid column experiences an extended trailing edge with a cusp-like shape and also exhibits a negative wake phenomena. However, a viscoelastic drop rising in a Newtonian fluid column develops an indentation around the rear stagnation point with a dimpled shape.

KEYWORDS

ALE approach, finite elements, Giesekus model, local projection stabilization, rising drop dynamics, viscoelastic fluids

1 | INTRODUCTION

Multiphase flows of two immiscible fluids are encountered in many industrial processes such as enhanced oil recovery, emulsions in colloid and interface science, polymer blends, droplet-based microfluidics, plastic profile extrusion, and medical applications in the case of blood pumps. Viscoelasticity plays a prominent role in the aforementioned applications. The fundamental understanding of the effects of viscoelasticity in multiphase flows is crucial as these effects directly impact the design and optimization of engineering processes subjected to complex interfacial flow dynamics. Therefore, scientific studies on a single liquid drop rising in a fluid column due to buoyancy with viscoelastic effects are highly demanded.

Due to the inherent complexity of viscoelastic fluids and the resulting analytic intractability of the mathematical models, theoretical predictions of rising viscoelastic drop behavior are very challenging or nearly impossible to obtain. The effects of viscoelasticity on the drop behavior have been investigated experimentally by a few researchers.[1-5] With recent advancement in numerical techniques and computational capabilities using high-performance computing, the use of high-fidelity numerical simulations is a useful and viable tool to understand the complex flow dynamics.

In spite of significant progress made in the development of numerical schemes for simulation of viscoelastic single-phase flows, computational methods for viscoelastic two-phase flows is gaining rapid attention only very recently.[6-10] Numerical computations of incompressible viscoelastic flows involve simultaneous solution of the Navier-Stokes equations and an equation for the evolution of viscoelastic stresses. Mathematical models for the evolution of viscoelastic stresses can be classified into two categories: kinetic theory models and continuum mechanics models. The kinetic theory approach attempts to model the polymer dynamics by using a coarse-grained description of polymer chains by representing them as chains of springs or rods, which eventually lead to the Fokker-Planck equation. Continuum approach attempts to provide constitutive differential equations, where the microproperties are obtained empirically. Oldroyd-B,[11] Giesekus,[12] finitely extensible nonlinear elastic (FENE-P,[13] FENE-CR[14]), Phan-Thien-Tanner,[15] and eXtended Pom-Pom[16] are the commonly used continuum models in the literature. In this study, we use the continuum models and in particular we consider the Giesekus constitutive model as it models shear thinning and elasticity together.

In addition to the challenges associated with the viscoelastic flows, the main challenge in the numerical simulation of interface flows is the tracking/capturing of the moving interface. Popular interface tracking/capturing methods in the literature are volume-of-fluid,[17] level set,[18,19] front-tracking,[20] boundary integral,[21] immersed boundary,[22] diffuse interface,[23] and arbitrary Lagrangian-Eulerian (ALE).[24-26] Furthermore, precise inclusion of the interfacial tension force and the local curvature on the interface is very challenging. Moreover, care needs to be taken to handle the jumps in the material properties (viscosity, density, relaxation time of polymers) across the interface. Most importantly the numerical scheme should not induce spurious velocities and should conserve the mass. Furthermore, the advective nature of the viscoelastic constitutive equation becomes dominant when the Weissenberg number (measure of the elasticity of fluid) is high. It necessitates the use of an accurate and robust stabilized numerical scheme to avoid oscillations in the numerical solution.

We now briefly review some of the numerical schemes used to simulate viscoelastic two-phase flows and the list is not exhaustive. Pillapakkam et al[27,28] developed a finite element code based on level-set method to examine the transient motion of drops rising in a viscoelastic liquid modeled by the Oldroyd-B equation. Furthermore, Chinyoka et al[29] investigated an Oldroyd-B droplet deforming under simple shear using volume-of-fluid and finite difference method. In addition, Habla et al[30] developed a volume-of-fluid methodology using the OpenFOAM CFD toolbox to simulate transient and steady-state viscoelastic droplet flow in shear and elongational flows. Furthermore, Harvie et al[31] studied the dynamics of an Oldroyd-B droplet passing through a microfluidic contraction using volume-of-fluid and finite volume method. Moreover, Yue et al[32,33] introduced a phase-field method for computing interfacial dynamics in viscoelastic fluids using finite elements. In addition, Zhang et al[34] proposed a moving finite element method based on phase-field method to simulate interfacial dynamics of two-phase viscoelastic flows. You et al[35,36] proposed a finite volume based boundary-fitted grid method for computations of an axisymmetric bubble rising in viscoelastic fluids using FENE-CR model. Furthermore, Chung et al[37,38] implemented a finite element-front tracking method to understand the effects of viscoelasticity using Oldroyd-B model on drop deformation in simple shear and 5:1:5 planar contraction/expansion microchannels. In addition, Mukherjee and Sarkar[39,40] numerically investigated the deformation of an Oldroyd-B drop in a Newtonian fluid using a front-tracking finite difference method. Moreover, Zainali et al[9] presented an improved smoothed particle hydrodynamics method for simulation of a buoyancy driven Newtonian bubble rising in an Oldroyd-B fluid. Furthermore, Vahabi and Kamkari[10] developed a weakly compressible smoothed particle hydrodynamics method for simulating bubble rising in Giesekus fluids. In addition, Lind and Phillips[41] used a boundary element method to study the dynamics of rising gas bubbles. Moreover, Walters and Phillips[8] developed a nonsingular boundary element method for modeling bubble dynamics in viscoelastic fluids. Recently, Izbassarov and Muradoglu[6,42] proposed a front tracking method for the simulation of viscoelastic two-phase flow systems in a buoyancy and pressure driven flow through a capillary tube with/without sudden contraction and expansion using Oldroyd-B, FENE-CR, and FENE-MCR models.

In this article, we present an ALE based finite element scheme for computations of a buoyancy driven three-dimensional (3D)-axisymmetric drop rise in a fluid column with viscoelastic effects using Giesekus model. The choice of ALE approach avoids fast distortion of meshes, which is the case in Lagrangian method. Since, the interface is resolved by the computational mesh, the interfacial force, and the different material properties in different phases can be incorporated very accurately in the ALE approach. The spurious velocities, which might arise due to the approximation errors of the pressure and the interfacial force including the curvature approximation, can be suppressed by using this approach.[43] Furthermore, we use the tangential gradient operator technique to treat the local curvature in a semi-implicit manner[44] and it avoids explicit computation of the curvature. Moreover, in contrast to the standard approach of using the differential equations in the cylindrical coordinates and seeking a suitable variational form, we derive the 3D-axisymmetric weak form directly from the weak form in 3D-Cartesian coordinates, refer.[24,45] Since the advective nature of the viscoelastic constitutive equation becomes dominant when the Weissenberg number is high, an appropriate stabilized numerical scheme needs to be used. In the context of stabilization schemes for viscoelastic flows, several schemes such as the streamline upwind Petrov-Galerkin (SUPG) method,[46] discrete elastic viscous stress splitting,[47,48] discontinuous Galerkin method,[49] Galerkin least squares,[50] and variational multiscale method[51,52] have been proposed in the literature. Furthermore, log-conformation reformulation method[53] has also been used in several computations of viscoelastic two-phase flows. For a detailed literature survey on the various stabilization schemes proposed for the computations of viscoelastic fluid flows, we refer to Reference 54. Recently, a three-field local projection stabilized (LPS) finite element scheme for simulation of viscoelastic fluid flows in fixed domains has been presented by Venkatesan and Ganesan.[54] Furthermore, the LPS scheme proposed in Reference 54 was extended for simulation of impinging viscoelastic droplet (free-surface flow).[45] Later, LPS scheme was used for simulation of viscoelastic two-phase flows with insoluble surfactants.[55] In this work, we extend the LPS scheme proposed in Reference 54 for finite element computations of 3D-axisymmetric viscoelastic two-phase flows. LPS is used in the numerical scheme to handle the convective nature of the viscoelastic constitutive equation and to use equal order interpolation spaces for the velocity and the viscoelastic stress.

The novelty of the present work can be summarized as follows :

1. ALE approach with finite elements for 3D-axisymmetric viscoelastic two-phase flows
2. LPS method to handle the advective nature of viscoelastic flows with moving interface
3. The Giesekus constitutive model is used for understanding the rising drop phenomena with shear thinning and elastic effects
4. Comprehensive numerical investigation of the rising drop dynamics is performed with viscoelastic effects using the following metrics : drop shape, sphericity of drop, diameter of the drop at the axis of symmetry, kinetic energy, elastic energy, rise velocity, center of mass of the drop, and viscoelastic stress contours.

The numerical results based on the defined metrics can be used for benchmarking purposes similar to the Newtonian two-phase flows article.[56]

The article is organized as follows. The governing equations for buoyancy driven viscoelastic two-phase flows and its dimensionless form are presented in Section 2. Section 3 describes the proposed numerical scheme. We first introduce the ALE formulation for time-dependent domains and the governing equations are rewritten in the ALE frame. Furthermore, we derive the variational form of the model equations and its axisymmetric form using cylindrical coordinates. The spatial and temporal discretization used in the numerical scheme are then outlined. The linearization strategy and the linear elastic mesh update technique for handling the inner mesh points in the computational domain is then explained. Section 4 is concerned with the computational results. The numerical scheme is first validated for a Newtonian drop rising in a Newtonian fluid column using a benchmark configuration. Then, we perform a grid independence test for the same benchmark configuration. Furthermore, a comprehensive numerical investigation on the Newtonian drop rising in a viscoelastic fluid column and a viscoelastic drop rising in a Newtonian fluid column is presented. We examine the influence of the viscosity ratio, Newtonian solvent ratio, Giesekus mobility factor, and the Eötvös number on the rising drop dynamics. Finally, a brief summary of the proposed numerical scheme and the key observations are presented in Section 5.

2 | MATHEMATICAL MODEL

2.1 | Governing equations

We consider a two-phase viscoelastic flow (either phase can be viscoelastic) in a bounded domain $\Omega \subset \mathbb{R}^3$ with a Lipschitz continuous boundary $\partial\Omega$. We assume that the fluid is incompressible, immiscible, and the material properties such as

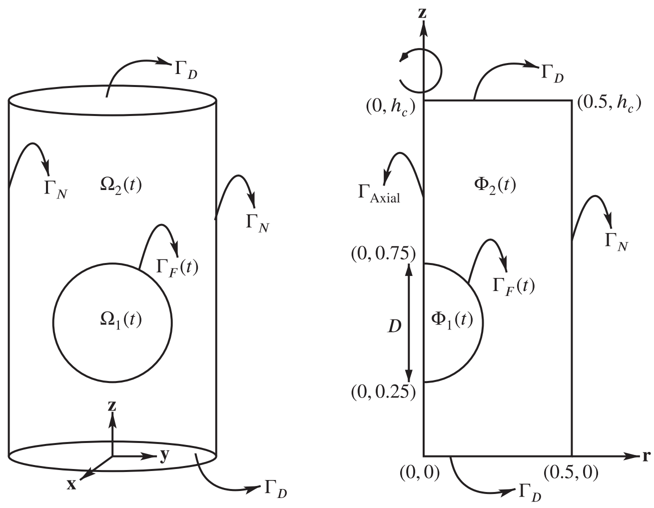

FIGURE 1 Computational model of viscoelastic two-phase flow

density, viscosity, and relaxation time of polymers in each fluid phase are constant. The schematic representation of the computational model is shown in Figure 1. The computational domain is denoted by $\Omega(t) := \Omega_1(t) \cup \Gamma_F(t) \cup \Omega_2(t)$, where a liquid droplet filling $\Omega_1(t)$ is completely surrounded by another liquid filling the domain $\Omega_2(t)$. Furthermore, the interface between the two liquids is denoted by $\Gamma_F(t)$, whereas Γ_{Axial}, Γ_D, and Γ_N denote the symmetry of axis, Dirichlet and Neumann boundaries, respectively. Note that the boundary of the computational domain $\Omega(t)$ is fixed over time. Herein, t is the time in a given time interval $[0, \mathrm{I}]$ with an end time I.

The fluid flow in $\Omega(t)$ is described by the time-dependent incompressible Navier-Stokes equations:

$$\begin{aligned} \rho_k \left(\frac{\partial \mathbf{u}}{\partial t} + (\mathbf{u} \cdot \nabla)\, \mathbf{u} \right) - \nabla \cdot \mathbb{T}_k(\mathbf{u}, p, \boldsymbol{\tau}_p) = \rho_k\, g\, \mathbf{e} \quad &\text{in} \quad \Omega_k(t) \times (0, \mathrm{I}], \\ \nabla \cdot \mathbf{u} = 0 \quad &\text{in} \quad \Omega_k(t) \times (0, \mathrm{I}], \end{aligned} \tag{1}$$

for $k = 1, 2$. Herein, $\mathbf{u}$ is the fluid velocity, p is the pressure in the fluid, $\boldsymbol{\tau}_p$ is the viscoelastic conformation stress, g is the gravitational constant, $\mathbf{e}$ is an unit vector in the direction of the gravitational force, and ρ_k is the density of fluid in $\Omega_k(t)$, $k = 1, 2$, respectively. For an incompressible viscoelastic fluid, the stress tensor $\mathbb{T}_k(\mathbf{u}, p, \boldsymbol{\tau}_p)$, and the velocity deformation tensor $\mathbb{D}(\mathbf{u})$ are given by

$$\mathbb{T}_k(\mathbf{u}, p, \boldsymbol{\tau}_p) = 2\mu_{s,k}\mathbb{D}(\mathbf{u}) - p\mathbb{I} + \frac{\mu_{p,k}}{\lambda_k}\left(\boldsymbol{\tau}_p - \mathbb{I}\right), \quad \mathbb{D}(\mathbf{u}) = \frac{1}{2}\left(\nabla \mathbf{u} + (\nabla \mathbf{u})^{\mathrm{T}}\right),$$

where $\mu_{s,k}$ is the Newtonian solvent viscosity, $\mu_{p,k}$ is the polymeric viscosity, $\mu_{0,k} = \mu_{s,k} + \mu_{p,k}$ is the total viscosity, $\mathbb{I}$ is the identity tensor, and λ_k is the relaxation time of the polymers in $\Omega_k(t)$, $k = 1, 2$, respectively.

The Giesekus model[12] is adopted as a constitutive equation for the viscoelastic stresses and it is given by

$$\frac{\partial \boldsymbol{\tau}_p}{\partial t} + (\mathbf{u} \cdot \nabla)\, \boldsymbol{\tau}_p - (\nabla \mathbf{u})^{\mathrm{T}} \cdot \boldsymbol{\tau}_p - \boldsymbol{\tau}_p \cdot \nabla \mathbf{u} + \frac{1}{\lambda_k}\left[\left(\boldsymbol{\tau}_p - \mathbb{I}\right) + \alpha_k\left(\boldsymbol{\tau}_p - \mathbb{I}\right)^2\right] = 0 \quad \text{in} \quad \Omega_k(t) \times (0, \mathrm{I}], \tag{2}$$

for $k = 1, 2$, where α_k is the Giesekus mobility factor. Note that, one can obtain the Oldroyd-B constitutive equation[11] by setting the Giesekus mobility parameter to zero, that is, $\alpha_k = 0$ in (2). The coupled Navier-Stokes (1) and Giesekus constitutive (2) equations are closed with initial and boundary conditions. At time $t = 0$, we specify the conformation stress tensor $\boldsymbol{\tau}_{p,0}$ and the divergence-free velocity field $\mathbf{u}_0$ over the entire computational domain Ω_0, that is,

$$\Omega(0) = \Omega_0, \quad \mathbf{u}(\cdot, 0) = \mathbf{u}_0 \text{ in } \Omega_0, \quad \boldsymbol{\tau}_p(\cdot, 0) = \boldsymbol{\tau}_{p,0} \text{ in } \Omega_0.$$

On the interface $\Gamma_F(t)$, we impose the kinematic condition

$$\mathbf{u} \cdot \boldsymbol{\nu}_F = \mathbf{w} \cdot \boldsymbol{\nu}_F \quad \text{on} \quad \Gamma_F(t) \times (0, \mathrm{I}], \tag{3}$$

and force balancing conditions

$$[|\mathbf{u}|] = 0, \quad [|\mathbb{T}(\mathbf{u}, p, \boldsymbol{\tau}_p)|] \cdot \boldsymbol{\nu}_F = \nabla_{\Gamma_F} \cdot \mathbb{S}_{\Gamma_F} \quad \text{on} \quad \Gamma_F(t) \times (0, \mathrm{I}].$$

Herein, $\mathbf{w}$ is the domain velocity, $\boldsymbol{\nu}_F$ is an unit normal vector on $\Gamma_F(t)$, and $[|\cdot|]$ denotes the jump of a function at the interface. Furthermore, we define the surface gradient of a scalar function ψ and the surface divergence of a vector function $\mathbf{v}$ on the interface $\Gamma_F(t)$ by

$$\nabla_{\Gamma_{\nu_F}} \psi = \mathbb{P}_{\nu_F} \nabla \psi, \quad \nabla_{\Gamma_{\nu_F}} \cdot \mathbf{v} = \mathrm{tr}\left(\mathbb{P}_{\nu_F} \nabla \mathbf{v}\right),$$

where $\mathbb{P}_{\nu_F} = \mathbb{I} - \boldsymbol{\nu}_F \otimes \boldsymbol{\nu}_F$ is the projection onto the tangential plane of $\Gamma_F(t)$. The interface stress tensor $\mathbb{S}_{\Gamma_F}$ is modeled by $\mathbb{S}_{\Gamma_F} = \sigma \mathbb{P}_{\nu_F}$, where σ is the interfacial tension.[44] Next, we assume that the boundary $\partial\Omega := \Gamma_D \cup \Gamma_N$ of the computational domain $\Omega(t)$ is fixed in time and we impose the no-slip condition

$$\mathbf{u} = 0 \quad \text{on} \quad \Gamma_D \times (0, \mathrm{I}],$$

and the free-slip condition

$$\boldsymbol{\tau}_N \cdot \mathbb{T}_2(\mathbf{u}, p, \boldsymbol{\tau}_p) \cdot \boldsymbol{\nu}_N = 0, \quad \mathbf{u} \cdot \boldsymbol{\nu}_N = 0 \quad \text{on} \quad \Gamma_N \times (0, \mathrm{I}], \tag{4}$$

where $\boldsymbol{\tau}_N$ and $\boldsymbol{\nu}_N$ are unit tangential and normal vectors, respectively, on Γ_N.

2.2 | Nondimensional form of the governing equations

Let L and U_∞ be the characteristic values of the length and velocity, respectively. We now define the following dimensionless variables

$$\tilde{x} = \frac{x}{\mathrm{L}}, \quad \tilde{\mathbf{u}} = \frac{\mathbf{u}}{\mathrm{U}_\infty}, \quad \tilde{\mathbf{w}} = \frac{\mathbf{w}}{\mathrm{U}_\infty}, \quad \tilde{t} = \frac{t\mathrm{U}_\infty}{\mathrm{L}}, \quad \tilde{p} = \frac{p}{\rho_2 \mathrm{U}_\infty^2}, \quad \tilde{I} = \frac{I\mathrm{U}_\infty}{\mathrm{L}}, \quad \tilde{\boldsymbol{\tau}}_p = \boldsymbol{\tau}_p, \quad \varepsilon = \frac{\mu_{0,2}}{\mu_{0,1}}.$$

Herein, ε is the ratio between the total viscosity of outer and inner phases. In addition, we define the nondimensional density ρ, Newtonian solvent ratio β, Giesekus mobility factor α, Reynolds number Re, and Weissenberg number Wi as

$$\rho(\mathbf{x}) = \begin{cases} \rho_1/\rho_2 & \forall\, \mathbf{x} \in \Omega_1(t), \\ 1 & \forall\, \mathbf{x} \in \Omega_2(t), \end{cases} \quad \beta(\mathbf{x}) = \begin{cases} \beta_1 = \mu_{s,1}/\mu_{0,1} & \forall\, \mathbf{x} \in \Omega_1(t), \\ \beta_2 = \mu_{s,2}/\mu_{0,2} & \forall\, \mathbf{x} \in \Omega_2(t), \end{cases} \quad \alpha(\mathbf{x}) = \begin{cases} \alpha_1 & \forall\, \mathbf{x} \in \Omega_1(t), \\ \alpha_2 & \forall\, \mathbf{x} \in \Omega_2(t), \end{cases}$$

$$\mathrm{Re}(\mathbf{x}) = \begin{cases} \varepsilon \mathrm{Re}_2 & \forall\, \mathbf{x} \in \Omega_1(t), \\ \mathrm{Re}_2 & \forall\, \mathbf{x} \in \Omega_2(t), \end{cases} \quad \mathrm{Re}_2 = \frac{\rho_2 \mathrm{U}_\infty \mathrm{L}}{\mu_{0,2}}, \quad \mathrm{Wi}(\mathbf{x}) = \begin{cases} \mathrm{Wi}_1 = \lambda_1 \mathrm{U}_\infty/\mathrm{L} & \forall\, \mathbf{x} \in \Omega_1(t), \\ \mathrm{Wi}_2 = \lambda_2 \mathrm{U}_\infty/\mathrm{L} & \forall\, \mathbf{x} \in \Omega_2(t), \end{cases}.$$

Using these nondimensional parameters in the governing equations and omitting the tilde afterward, we obtain the dimensionless form of the governing equations for the two-phase viscoelastic flow as

$$\begin{aligned} \rho\left(\frac{\partial \mathbf{u}}{\partial t} + (\mathbf{u} \cdot \nabla)\, \mathbf{u}\right) - \nabla \cdot \mathbb{T}(\mathbf{u}, p, \boldsymbol{\tau}_p) &= \frac{\rho\, \mathbf{e}}{\mathrm{Fr}} && \text{in } \Omega(t) \times (0, \mathrm{I}], \\ \nabla \cdot \mathbf{u} &= 0 && \text{in } \Omega(t) \times (0, \mathrm{I}], \\ \frac{\partial \boldsymbol{\tau}_p}{\partial t} + (\mathbf{u} \cdot \nabla)\, \boldsymbol{\tau}_p - (\nabla \mathbf{u})^{\mathrm{T}} \cdot \boldsymbol{\tau}_p - \boldsymbol{\tau}_p \cdot \nabla \mathbf{u} + \frac{1}{\mathrm{Wi}}\left[\left(\boldsymbol{\tau}_p - \mathbb{I}\right) + \alpha\left(\boldsymbol{\tau}_p - \mathbb{I}\right)^2\right] &= 0 && \text{in } \Omega(t) \times (0, \mathrm{I}], \\ \mathbf{u} \cdot \boldsymbol{\nu}_F = \mathbf{w} \cdot \boldsymbol{\nu}_F, \quad [|\mathbb{T}(\mathbf{u}, p, \boldsymbol{\tau}_p)|] \cdot \boldsymbol{\nu}_F = \frac{1}{\mathrm{We}} \nabla_{\Gamma_{\nu_F}} \cdot \mathbb{P}_{\nu_F}, \quad [|\mathbf{u}|] &= 0 && \text{on } \Gamma_F(t) \times (0, \mathrm{I}], \\ \mathbf{u} &= 0 && \text{on } \Gamma_D \times (0, \mathrm{I}], \\ \boldsymbol{\tau}_N \cdot \mathbb{T}_2(\mathbf{u}, p, \boldsymbol{\tau}_p) \cdot \boldsymbol{\nu}_N = 0, \quad \mathbf{u} \cdot \boldsymbol{\nu}_N &= 0 && \text{on } \Gamma_N \times (0, \mathrm{I}], \end{aligned} \tag{5}$$

with the dimensionless numbers (Froude and Weber numbers, respectively)

$$\mathrm{Fr} = \frac{\mathrm{U}_\infty^2}{\mathrm{Lg}}, \quad \mathrm{We} = \frac{\rho_2 \mathrm{U}_\infty^2 \mathrm{L}}{\sigma},$$

and the dimensionless stress tensor

$$\mathbb{T}(\mathbf{u}, p, \boldsymbol{\tau}_p) = \frac{2\beta}{\mathrm{Re}} \mathbb{D}(\mathbf{u}) - p\mathbb{I} + \frac{(1-\beta)}{\mathrm{ReWi}} \left(\boldsymbol{\tau}_p - \mathbb{I}\right).$$

Often the characteristic value of the velocity in interface flows is chosen as $\mathrm{U}_\infty = \sqrt{\mathrm{Lg}}$ and in this case, the Weber number will become Eötvös number,

$$\mathrm{Eo} = \frac{\rho_2 \mathrm{g} \mathrm{L}^2}{\sigma},$$

and the Froude number will reduce to one.

3 | NUMERICAL SCHEME

3.1 | ALE formulation for time-dependent domain

The time-dependent subdomains and the interface are tracked using the ALE approach with moving meshes. Let $\hat{\Omega} := \hat{\Omega}_1 \cup \hat{\Gamma}_F \cup \hat{\Omega}_2$ be a reference domain of $\Omega(t)$ and then, we define a family of ALE mappings

$$\mathcal{A}_t : \hat{\Omega} \to \Omega(t), \qquad \mathcal{A}_t(\mathbf{Y}) = \mathbf{X}(\mathbf{Y}, t), \qquad t \in (0, \mathrm{I}),$$

where $\mathbf{X} \in \Omega(t)$ and $\mathbf{Y} \in \hat{\Omega}$ are the Eulerian and ALE coordinates, respectively. In computations, we take the previous time-step domain as the reference domain. To rewrite the model equations into a nonconservative ALE form, the time derivative has to be replaced with the time derivative on the reference frame and it results in an addition of convective mesh velocity term in the equations, for more details we refer to References 24,44,45. Incorporating it, the ALE form of the time-dependent Navier-Stokes equations can be written as:

$$\nabla \cdot \mathbf{u} = 0, \quad \rho \left(\frac{\partial \mathbf{u}}{\partial t} |_{\hat{\Omega}} + ((\mathbf{u} - \mathbf{w}) \cdot \nabla)\, \mathbf{u} \right) - \nabla \cdot \mathbb{T}(\mathbf{u}, p, \boldsymbol{\tau}_p) = \frac{\rho\, \mathbf{e}}{\mathrm{Fr}} \quad \text{in } \Omega(t) \times (0, \mathrm{I}], \tag{6}$$

whereas, the ALE form of the Giesekus constitutive equation is given by

$$\left.\frac{\partial \boldsymbol{\tau}_p}{\partial t}\right|_{\hat{\Omega}} + ((\mathbf{u} - \mathbf{w}) \cdot \nabla)\, \boldsymbol{\tau}_p - (\nabla \mathbf{u})^{\mathrm{T}} \cdot \boldsymbol{\tau}_p - \boldsymbol{\tau}_p \cdot \nabla \mathbf{u} + \frac{1}{\mathrm{Wi}} \left[\left(\boldsymbol{\tau}_p - \mathbb{I}\right) + \alpha \left(\boldsymbol{\tau}_p - \mathbb{I}\right)^2 \right] = 0 \quad \text{in } \Omega(t) \times (0, \mathrm{I}]. \tag{7}$$

Furthermore, we assume that the topology of the computational domain does not change during the computations.

3.2 | Variational formulation

Let $\mathrm{L}^2(\Omega(t))$ and $\mathrm{H}^1(\Omega(t))$ be the standard Sobolev spaces and $(\cdot,\cdot)$ be the inner product in $\mathrm{L}^2(\Omega(t))$ and its vector/tensor-valued versions, respectively. We define the velocity, pressure, and viscoelastic stress[57,58] spaces as

$$\begin{aligned}
V(\Omega(t)) &:= \left\{ \mathbf{v} \in \mathrm{H}^1(\Omega(t))^3 \ : \ \mathbf{v} \cdot \boldsymbol{\nu}_N = 0 \text{ on } \Gamma_N, \quad \mathbf{v} = 0 \text{ on } \Gamma_D \right\}, \\
Q(\Omega(t)) &:= \left\{ q \in \mathrm{L}^2(\Omega(t)) \ : \ \int_\Omega q \, dx = 0 \right\}, \\
S(\Omega(t)) &:= \left\{ \boldsymbol{\psi} = [\psi_{ij}], 1 \le i,j \le 3 \ : \ \psi_{ij} \in \mathrm{L}^2(\Omega(t)), \quad \psi_{ij} = \psi_{ji}, \quad \mathbf{v} \cdot \nabla \boldsymbol{\psi} \in \mathrm{L}^2(\Omega(t))^{3\times 3}_{\mathrm{sym}} \ \forall\, \mathbf{v} \in V \right\}.
\end{aligned}$$

We now multiply the ALE form of the mass and momentum balance Equation (6) by test functions $q \in Q$ and $\mathbf{v} \in V$, respectively and integrate over the computational domain $\Omega(t)$. Then, applying integration by parts to the stress tensor term over the subdomain $\Omega_1(t)$, we get

$$-\int_{\Omega_1(t)} \nabla \cdot \mathbb{T}_1(\mathbf{u}, p, \boldsymbol{\tau}_p) \cdot \mathbf{v}\, dx = \int_{\Omega_1(t)} \frac{2\beta}{\mathrm{Re}}\, \mathbb{D}(\mathbf{u}) : \mathbb{D}(\mathbf{v})\, dx - \int_{\Omega_1(t)} p\, (\nabla \cdot \mathbf{v})\, dx + \int_{\Omega_1(t)} \frac{(1-\beta)}{\mathrm{ReWi}}\, \boldsymbol{\tau}_p : \mathbb{D}(\mathbf{v})\, dx + \int_{\Gamma_F(t)} \mathbf{v} \cdot \mathbb{T}_1(\mathbf{u}, p, \boldsymbol{\tau}_p) \cdot \boldsymbol{\nu}_F\, d\gamma_F, \tag{8}$$

and over the subdomain $\Omega_2(t)$, we obtain

$$-\int_{\Omega_2(t)} \nabla \cdot \mathbb{T}_2(\mathbf{u}, p, \boldsymbol{\tau}_p) \cdot \mathbf{v}\, dx = \int_{\Omega_2(t)} \frac{2\beta}{\mathrm{Re}} \mathbb{D}(\mathbf{u}) : \mathbb{D}(\mathbf{v})\, dx - \int_{\Omega_2(t)} p\, (\nabla \cdot \mathbf{v})\, dx + \int_{\Omega_2(t)} \frac{(1-\beta)}{\mathrm{ReWi}} \boldsymbol{\tau}_p : \mathbb{D}(\mathbf{v})\, dx - \int_{\partial\Omega_2(t)} \mathbf{v} \cdot \mathbb{T}_2(\mathbf{u}, p, \boldsymbol{\tau}_p) \cdot \boldsymbol{\nu}\, d\gamma. \tag{9}$$

Rewriting the boundary integral in (9) into integral over Γ_D, Γ_N, and $\Gamma_F(t)$, we get

$$-\int_{\partial\Omega_2(t)} \mathbf{v} \cdot \mathbb{T}_2(\mathbf{u}, p, \boldsymbol{\tau}_p) \cdot \boldsymbol{\nu}\, d\gamma = -\int_{\Gamma_D} \mathbf{v} \cdot \mathbb{T}_2(\mathbf{u}, p, \boldsymbol{\tau}_p) \cdot \boldsymbol{\nu}_D\, d\gamma_D - \int_{\Gamma_N} \mathbf{v} \cdot \mathbb{T}_2(\mathbf{u}, p, \boldsymbol{\tau}_p) \cdot \boldsymbol{\nu}_N\, d\gamma_N - \int_{\Gamma_F(t)} \mathbf{v} \cdot \mathbb{T}_2(\mathbf{u}, p, \boldsymbol{\tau}_p) \cdot \boldsymbol{\nu}_F\, d\gamma_F. \tag{10}$$

Since the velocity space is chosen such that $\mathbf{v} = 0$ on Γ_D, the integral over Γ_D in (10) vanishes. Furthermore, using the orthonormal decomposition, we split the test function $\mathbf{v}$ as

$$\mathbf{v} = (\mathbf{v} \cdot \boldsymbol{\nu}_N)\, \boldsymbol{\nu}_N + (\mathbf{v} \cdot \boldsymbol{\tau}_N)\boldsymbol{\tau}_N,$$

in the integral over Γ_N in (10) and the integral becomes,

$$-\int_{\Gamma_N} \mathbf{v} \cdot \mathbb{T}_2(\mathbf{u}, p, \boldsymbol{\tau}_p) \cdot \boldsymbol{\nu}_N\, d\gamma_N = -\int_{\Gamma_N} (\mathbf{v} \cdot \boldsymbol{\nu}_N) \left(\boldsymbol{\nu}_N \cdot \mathbb{T}_2(\mathbf{u}, p, \boldsymbol{\tau}_p) \cdot \boldsymbol{\nu}_N \right)\, d\gamma_N - \int_{\Gamma_N} (\mathbf{v} \cdot \boldsymbol{\tau}_N) \left(\boldsymbol{\tau}_N \cdot \mathbb{T}_2(\mathbf{u}, p, \boldsymbol{\tau}_p) \cdot \boldsymbol{\nu}_N \right)\, d\gamma_N. \tag{11}$$

Since the velocity space is chosen such that $\mathbf{v} \cdot \boldsymbol{\nu}_N = 0$ on Γ_N, the first integral in (11) vanishes and further, incorporating the free slip condition (4), the second integral in (11) also vanishes. After summing up the interface $\Gamma_F(t)$ integrals in Equations (8) and (9), and further incorporating the force balancing condition (f*ourth* equation in (5)) and applying integration by parts, we obtain

$$\int_{\Gamma_F(t)} \mathbf{v} \cdot \mathbb{T}_1(\mathbf{u}, p, \boldsymbol{\tau}_p) \cdot \boldsymbol{\nu}_N\, d\gamma_F - \int_{\Gamma_F(t)} \mathbf{v} \cdot \mathbb{T}_2(\mathbf{u}, p, \boldsymbol{\tau}_p) \cdot \boldsymbol{\nu}_N\, d\gamma_F = -\int_{\Gamma_F(t)} \mathbf{v} \cdot [|\mathbb{T}(\mathbf{u}, p, \boldsymbol{\tau}_p)|] \cdot \boldsymbol{\nu}_N\, d\gamma_F = -\frac{1}{\mathrm{We}} \int_{\Gamma_F(t)} \mathbf{v} \cdot \left(\nabla_{\Gamma_{\nu_F}} \cdot \mathbb{P}_{\nu_F} \right)\, d\gamma_F = \frac{1}{\mathrm{We}} \int_{\Gamma_F(t)} \mathbb{P}_{\nu_F} : \left(\nabla_{\Gamma_{\nu_F}} \mathbf{v} \right)\, d\gamma_F. \tag{12}$$

Thus, the variational form of the Navier-Stokes equations read:
For given Ω_0, $\mathbf{u}_0/\mathrm{U}_\infty$, $\mathbf{w}$, $\boldsymbol{\tau}_{p,0}$, find $(\mathbf{u}, p) \in V \times Q$ such that

$$\left(\rho \frac{\partial \mathbf{u}}{\partial t}, \mathbf{v} \right)_{\hat{\Omega}} + a(\hat{\mathbf{u}} - \mathbf{w}; \mathbf{u}, \mathbf{v}) - b(p, \mathbf{v}) + c(\boldsymbol{\tau}_p, \mathbf{v}) = f_1(\mathbf{v}), \quad b(q, \mathbf{u}) = 0, \tag{13}$$

for all $(\mathbf{v}, q) \in V \times Q$, where

$$
\begin{aligned}
a(\hat{\mathbf{u}}-\mathbf{w};\mathbf{u},\mathbf{v}) &= \int_{\Omega(t)} \rho\,(((\hat{\mathbf{u}}-\mathbf{w})\cdot\nabla)\,\mathbf{u})\cdot\mathbf{v}\;dx + \int_{\Omega(t)} \frac{2\beta}{\mathrm{Re}}\,\mathbb{D}(\mathbf{u}) : \mathbb{D}(\mathbf{v})\;dx\\
b(q,\mathbf{v}) &= \int_{\Omega(t)} q\,(\nabla\cdot\mathbf{v})\;dx\\
c(\boldsymbol{\tau}_p,\mathbf{v}) &= \int_{\Omega(t)} \frac{(1-\beta)}{\mathrm{ReWi}}\;\boldsymbol{\tau}_p : \mathbb{D}(\mathbf{v})\;dx\\
f_1(\mathbf{v}) &= \frac{1}{\mathrm{Fr}}\int_{\Omega(t)} \rho\,(\mathbf{e}\cdot\mathbf{v})\;dx - \frac{1}{\mathrm{We}}\int_{\Gamma_F(t)} \mathbb{P}_{\boldsymbol{\nu}_F} : \left(\nabla_{\Gamma_{\boldsymbol{\nu}_F}}\mathbf{v}\right)\;d\gamma_F.
\end{aligned}
$$

Next, to derive a variational form of the Giesekus equation, we multiply the ALE form of Giesekus Equation (7) by a test function $\boldsymbol{\psi} \in S$ and integrate over the computational domain $\Omega(t)$. The variational form of the Giesekus equation read:

For given Ω_0, $\mathbf{u}_0/\mathrm{U}_\infty$, $\mathbf{w}$, $\boldsymbol{\tau}_{p,0}$, find $\boldsymbol{\tau}_p \in S$ such that

$$
\left(\frac{\partial\boldsymbol{\tau}_p}{\partial t},\boldsymbol{\psi}\right)_{\hat{\Omega}} + d(\hat{\mathbf{u}}-\mathbf{w};\boldsymbol{\tau}_p,\boldsymbol{\psi}) + e(\hat{\boldsymbol{\tau}}_p;\boldsymbol{\tau}_p,\boldsymbol{\psi}) = f_2(\boldsymbol{\psi}), \tag{14}
$$

for all $\boldsymbol{\psi} \in S$, where

$$
\begin{aligned}
d(\hat{\mathbf{u}}-\mathbf{w};\boldsymbol{\tau}_p,\boldsymbol{\psi}) &= \int_{\Omega(t)} \left(((\hat{\mathbf{u}}-\mathbf{w})\cdot\nabla)\,\boldsymbol{\tau}_p\right) : \boldsymbol{\psi}\;dx - \int_{\Omega(t)} \left((\nabla\hat{\mathbf{u}})^{\mathrm{T}}\cdot\boldsymbol{\tau}_p + \boldsymbol{\tau}_p\cdot(\nabla\hat{\mathbf{u}})\right) : \boldsymbol{\psi}\;dx\\
e(\hat{\boldsymbol{\tau}}_p;\boldsymbol{\tau}_p,\boldsymbol{\psi}) &= \int_{\Omega(t)} \frac{\alpha}{\mathrm{Wi}}\;\left(\hat{\boldsymbol{\tau}}_p\cdot\boldsymbol{\tau}_p\right) : \boldsymbol{\psi}\;dx + \int_{\Omega(t)} \frac{(1-2\alpha)}{\mathrm{Wi}}\;\boldsymbol{\tau}_p : \boldsymbol{\psi}\;dx\\
f_2(\boldsymbol{\psi}) &= \int_{\Omega(t)} \frac{(1-\alpha)}{\mathrm{Wi}}\;\mathbb{I} : \boldsymbol{\psi}\;dx.
\end{aligned}
$$

Since the coupled two-phase viscoelastic flow system is solved in a monolithic approach, we rewrite the variational formulations (13) and (14) as follows:

For given Ω_0, $\mathbf{u}_0/\mathrm{U}_\infty$, $\mathbf{w}$, and $\boldsymbol{\tau}_{p,0}$, find $(\mathbf{u}, p, \boldsymbol{\tau}_p) \in V \times Q \times S$ such that

$$
\left(\rho\frac{\partial\mathbf{u}}{\partial t},\mathbf{v}\right)_{\hat{\Omega}} + \left(\frac{\partial\boldsymbol{\tau}_p}{\partial t},\boldsymbol{\psi}\right)_{\hat{\Omega}} + A(((\hat{\mathbf{u}}-\mathbf{w}),\hat{\boldsymbol{\tau}}_p);(\mathbf{u},p,\boldsymbol{\tau}_p),(\mathbf{v},q,\boldsymbol{\psi})) = f_1(\mathbf{v}) + f_2(\boldsymbol{\psi}), \tag{15}
$$

for all $(\mathbf{v}, q, \boldsymbol{\psi}) \in V \times Q \times S$, where

$$
A(((\hat{\mathbf{u}}-\mathbf{w}),\hat{\boldsymbol{\tau}}_p);(\mathbf{u},p,\boldsymbol{\tau}_p),(\mathbf{v},q,\boldsymbol{\psi})) = a(\hat{\mathbf{u}}-\mathbf{w};\mathbf{u},\mathbf{v}) - b(p,\mathbf{v}) + c(\boldsymbol{\tau}_p,\mathbf{v}) + b(q,\mathbf{u}) + d(\hat{\mathbf{u}}-\mathbf{w};\boldsymbol{\tau}_p,\boldsymbol{\psi}) + e(\hat{\boldsymbol{\tau}}_p;\boldsymbol{\tau}_p,\boldsymbol{\psi}).
$$

3.3 | 3D-axisymmetric formulation

The considered domain is rotational symmetric and thus we consider a two-dimensional (2D) meridian domain $\Phi(t)$ of $\Omega(t)$ with a 3D-axisymmetric configuration. The axisymmetric formulation allows us to reduce the space dimension of the problem by one and hence, we use 2D finite elements for approximating the velocity, pressure, and viscoelastic stress. Furthermore, the computational cost and complexity of mesh movement will drastically be reduced by using the 3D-axisymmetric formulation. In the meridian domain Φ(t), the unknown components of the velocity and the symmetric viscoelastic conformation stress tensor are given by

$$
\mathbf{u} = (u_r, u_z)^{\mathrm{T}} \quad \text{and} \quad \boldsymbol{\tau}_p = \begin{bmatrix} \tau_{rr} & \tau_{rz}\\ \tau_{zr} & \tau_{zz} \end{bmatrix} \quad \text{with } \tau_{zr} = \tau_{rz}.
$$

The boundary of the meridian domain $\Phi(t)$ is given by $\partial\Phi_1(t) := \Gamma_F(t) \cup \Gamma_{\text{Axial}}$ and $\partial\Phi_2(t) := \Gamma_F(t) \cup \Gamma_{\text{Axial}} \cup \Gamma_D \cup \Gamma_N$. By contrast to the standard approach of starting with the differential equations in cylindrical coordinate form and deriving a suitable variational formulation, we derive the 3D-axisymmetric weak form in the meridian domain $\Phi(t)$ directly from the weak form (15) defined in 3D-Cartesian coordinates. To achieve this, we transform the volume and surface integrals in (15) into area and line integrals by introducing cylindrical coordinates and imposing irrotational, axisymmetric conditions as described in References 24,45. This approach leads naturally to boundary conditions along the rotational axis

$$u_r = 0, \quad \frac{\partial u_z}{\partial r} = 0 \quad \text{on} \quad \Gamma_{\text{Axial}}(t), \tag{16}$$

which are already partly included in the weak form. Furthermore, we define the velocity, pressure and viscoelastic conformation stress spaces in the 2D meridian domain $\Phi(t)$ as

$$\begin{aligned}
\tilde{V}(\Phi(t)) &:= \left\{ \mathbf{v} \in \mathrm{H}^1(\Phi(t))^2 \;:\; \mathbf{v}\cdot\boldsymbol{\nu}_N = 0 \text{ on } \Gamma_N, \quad \mathbf{v} = 0 \text{ on } \Gamma_D, \quad v_r = 0 \text{ on } \Gamma_{\text{Axial}} \right\},\\
\tilde{Q}(\Phi(t)) &:= \left\{ q \in \mathrm{L}^2(\Phi(t)) \;:\; \int_\Omega q\, dx = 0 \right\},\\
\tilde{S}(\Phi(t)) &:= \left\{ \boldsymbol{\psi} = [\psi_{ij}], 1 \le i,j \le 2 \;:\; \psi_{ij} \in \mathrm{L}^2(\Phi(t)), \quad \psi_{ij} = \psi_{ji} \quad \mathbf{v}\cdot\nabla\boldsymbol{\psi} \in \mathrm{L}^2(\Omega(t))^{2\times 2}_{\text{sym}} \;\; \forall \;\; \mathbf{v} \in V \right\}.
\end{aligned}$$

3.4 | Spatial and temporal discretization

Let $\{\mathcal{T}_h\}$ be a partition of the meridian domain $\Phi(t)$ into an interface-resolved triangular mesh using the mesh generator Triangle.[59,60] The diameter of a cell $K \in \mathcal{T}_h$ is denoted by h_K. The mesh parameter h is defined by $h = \max\{h_K \mid K \in \mathcal{T}_h\}$. The discrete form of the meridian domain Φ is given by $\Phi_h := \cup_{K\in\mathcal{T}_h} K$, whereas $\hat{\Phi}_h$ denotes the reference domain of Φ_h. Furthermore, let $V_h \subset \tilde{V}$, $Q_h \subset \tilde{Q}$, and $S_h \subset \tilde{S}$ be the conforming finite element spaces on $\mathcal{T}_h$. The standard Galerkin finite element approximation of the variational problem (15) reads:

For given Φ_0, $\mathbf{u}_0/\mathrm{U}_\infty$, $\mathbf{w}_h$, and $\boldsymbol{\tau}_{p,0}$, find $(\mathbf{u}_h, p_h, \boldsymbol{\tau}_{p,h}) \in V_h \times Q_h \times S_h$ such that

$$\left(\rho\frac{\partial \mathbf{u}_h}{\partial t}, \mathbf{v}_h\right)_{\hat{\Phi}_h} + \left(\frac{\partial \boldsymbol{\tau}_{p,h}}{\partial t}, \boldsymbol{\psi}_h\right)_{\hat{\Phi}_h} + A(((\hat{\mathbf{u}}_h - \mathbf{w}_h), \hat{\boldsymbol{\tau}}_{p,h}); (\mathbf{u}_h, p_h, \boldsymbol{\tau}_{p,h}), (\mathbf{v}_h, q_h, \boldsymbol{\psi}_h)) = f_1(\mathbf{v}_h) + f_2(\boldsymbol{\psi}_h), \tag{17}$$

for all $(\mathbf{v}_h, q_h, \boldsymbol{\psi}_h) \in V_h \times Q_h \times S_h$. Herein, $(\cdot,\cdot)$ denotes the inner product in $\mathrm{L}^2(\Phi(t))$ and its vector/tensor valued versions, respectively. The choice of finite element spaces for the velocity, pressure, and viscoelastic stress is subject to the following two inf-sup conditions,

$$\inf_{q_h\in Q_h}\sup_{\mathbf{v}_h\in V_h} \frac{(q_h, \nabla\cdot\mathbf{v}_h)}{\|q_h\|_{Q_h}\|\mathbf{v}_h\|_{V_h}} \ge \zeta_1 > 0, \qquad \inf_{\mathbf{v}_h\in V_h}\sup_{\boldsymbol{\tau}_{p,h}\in S_h} \frac{\left(\boldsymbol{\tau}_{p,h}, \mathbb{D}(\mathbf{v}_h)\right)}{\|\boldsymbol{\tau}_{p,h}\|_{S_h}\|\mathbf{v}_h\|_{V_h}} \ge \zeta_2 > 0. \tag{18}$$

The standard Galerkin approach for solving the coupled Navier-Stokes and Giesekus constitutive problem may suffer in general from two shortcomings. First, the constitutive equation is highly advection dominated at high Weissenberg numbers. Second, the finite element spaces should satisfy these two discrete inf-sup conditions (18) simultaneously to have a control over p_h and $\mathbb{D}(\mathbf{u}_h)$. One way to overcome these difficulties is to use a stabilized formulation. In this work, we add symmetric stabilization terms to the standard Galerkin formulation (17) by using one-level LPS method. LPS was initially proposed for the Stokes problem by Becker and Braack,[61] and later it has been extended for transport[62] and Oseen[63] problems. Recently, LPS technique has been used by Venkatesan and Ganesan[45,54] for the simulation of viscoelastic fluid flows. The one-level LPS scheme[54,64-66] is based on enrichment of approximation spaces and it allows us to perform the computations on a single mesh as the approximation and the projection spaces are defined on the same mesh. We use mapped finite element spaces in the computations, where the enriched approximation spaces on the reference cell $\hat{K}$ are given by

$$P_r^{\text{bubble}}\left(\hat{K}\right) := P_r\left(\hat{K}\right) \oplus \left(\hat{b}_\triangle \cdot P_{r-1}\left(\hat{K}\right)\right),$$

with $r \geq 2$. Herein, $\hat{b}_{\triangle}$ is a cubic polynomial bubble function on the reference triangle and P_r is a conforming finite element space of polynomial of degree r on $\hat{K}$.

Let Y_h denote the approximation space and D_h be the discontinuous projection space defined on $\mathcal{T}_h$. Let $D_h(K) := \{d_h|_K : d_h \in D_h\}$ and $\pi_K : Y_h(K) \to D_h(K)$ be the local L^2-projection into $D_h(K)$. Furthermore, we define the global projection $\pi_h : Y_h \to D_h$ by $(\pi_h y)|_K := \pi_K(y|_K)$. The fluctuation operator $\kappa_h : Y_h \to Y_h$ is given by $\kappa_h := id - \pi_h$, where id is the identity mapping. We apply these operators to vector/tensor valued functions in a component-wise manner. Adding symmetric stabilization terms to the variational problem (17), leads to the following variational form:

For given Φ_0, $\mathbf{u}_0/\mathrm{U}_\infty$, $\mathbf{w}_h$, and $\boldsymbol{\tau}_{p,0}$, find $(\mathbf{u}_h, p_h, \boldsymbol{\tau}_{p,h}) \in V_h \times Q_h \times S_h$ such that

$$\begin{aligned}&\left(\rho \frac{\partial \mathbf{u}_h}{\partial t}, \mathbf{v}_h\right)_{\hat{\Phi}_h} + \left(\frac{\partial \boldsymbol{\tau}_{p,h}}{\partial t}, \boldsymbol{\psi}_h\right)_{\hat{\Phi}_h} + A(((\hat{\mathbf{u}}_h - \mathbf{w}_h), \hat{\boldsymbol{\tau}}_{p,h}); (\mathbf{u}_h, p_h, \boldsymbol{\tau}_{p,h}), (\mathbf{v}_h, q_h, \boldsymbol{\psi}_h)) \\ &\quad + S_1(\mathbf{u}_h, \mathbf{v}_h) + S_2(\boldsymbol{\tau}_{p,h}, \boldsymbol{\psi}_h) = f_1(\mathbf{v}_h) + f_2(\boldsymbol{\psi}_h),\end{aligned} \tag{19}$$

for all $(\mathbf{v}_h, q_h, \boldsymbol{\psi}_h) \in V_h \times Q_h \times S_h$, where

$$\begin{aligned}S_1(\mathbf{u}_h, \mathbf{v}_h) &= \sum_{K \in \mathcal{T}_h} \varsigma_1 \langle \kappa_h \mathbb{D}(\mathbf{u}_h), \kappa_h \mathbb{D}(\mathbf{v}_h) \rangle_K, \\ S_2(\boldsymbol{\tau}_{p,h}, \boldsymbol{\psi}_h) &= \sum_{K \in \mathcal{T}_h} \varsigma_2 \left\langle \kappa_h \left(\nabla \cdot \boldsymbol{\tau}_{p,h}\right), \kappa_h \left(\nabla \cdot \boldsymbol{\psi}_h\right) \right\rangle_K + \sum_{K \in \mathcal{T}_h} \varsigma_3 \left\langle \kappa_h \nabla \boldsymbol{\tau}_{p,h}, \kappa_h \nabla \boldsymbol{\psi}_h \right\rangle_K.\end{aligned}$$

Herein, $\varsigma_1 = (1-\beta)c_1 h_K$, $\varsigma_2 = c_2 h_K$, $\varsigma_3 = c_3 h_K$, with c_1, c_2, and c_3 being user-chosen constants. There are a few expressions for optimal choice of stabilization parameters in SUPG-based stabilization for convection-diffusion problems, refer.[67] However, there is not any expression for the choice of stabilization constants in LPS-based stabilization in the literature and it needs a detailed theoretical investigation. In computations, we choose these constants based on stability considerations and observations from numerical results. The term $S_1(\mathbf{u}_h, \mathbf{v}_h)$ provides control when the elastic contribution is high, that is, when β is small. The first term in $S_2(\boldsymbol{\tau}_{p,h}, \boldsymbol{\psi}_h)$ provides control on the divergence of the conformation stress and it allows to use equal order interpolation spaces for the velocity and the conformation stress. The second term in $S_2(\boldsymbol{\tau}_{p,h}, \boldsymbol{\psi}_h)$ ensures the stability of the constitutive equation in advection dominated case. Furthermore, we use inf-sup stable finite element pairs for the velocity and pressure spaces, thereby ensuring we do not require an additional stabilizing term for the pressure. For more details on LPS for viscoelastic fluid flows we refer to References 45,54.

The finite elements should be chosen in such a way that the mass should be conserved well and spurious velocities, if there are any should be suppressed.[43] Hence, we use the following triplet $(V_h, Q_h, S_h) = \left(P_2^{\text{bubble}}, P_1^{\text{disc}}, P_2^{\text{bubble}}\right)$, see Figure 2. The set of nodal functionals for the finite element space P_1^{disc} is given by

$$\hat{N}_K^{\text{disc}} = \left\{\hat{N}_1^{\text{disc}}, \hat{N}_2^{\text{disc}}, \hat{N}_3^{\text{disc}}\right\}$$

$$\hat{N}_1^{\text{disc}}(p) = \tfrac{1}{|\hat{K}|}\int_{\hat{K}} p(\hat{X})\, d\hat{X}, \hat{N}_2^{\text{disc}}(p) = \tfrac{1}{|\hat{K}|}\int_{\hat{K}} \left(\hat{x} - \tfrac{1}{3}\right)\, p(\hat{X})\, d\hat{X}, \quad \hat{N}_3^{\text{disc}}(p) = \tfrac{1}{|\hat{K}|}\int_{\hat{K}} \left(\hat{y} - \tfrac{1}{3}\right)\, p(\hat{X})\, d\hat{X}. \tag{20}$$

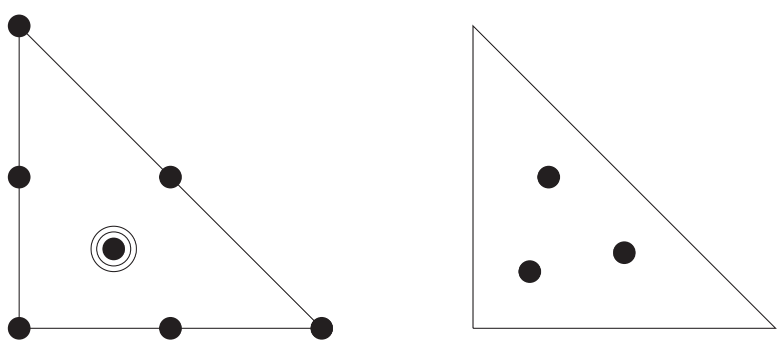

FIGURE 2 Degrees of freedom of conforming P_2^{bubble} (left) and discontinuous P_1^{disc} (right) finite element on a reference triangle

Furthermore, the local shape functions for the space P_1^{disc} are given by

$$\{1,\ \hat{x}+\hat{y}/2-1/2, \hat{x}/2+\hat{y}-1/2\}.$$

By using discontinuous pressure approximation on interface-resolved meshes, spurious velocities can be avoided during the computations.[43] Moreover, the first integral moments of the divergence of velocity field vanishes element wise with discontinuous pressure approximation and it leads to a better mass conservation. Furthermore, in order to suppress the spurious velocities generated by the curvature approximation error, we use the tangential gradient operator technique with isoparametric finite elements for velocity approximation.

Let $0=t^0<t^1<\ldots<t^N=I$ be a decomposition of the time interval $[0,\mathrm{I}]$, and $\delta t=t^{n+1}-t^n$, $n=0,\ldots,N-1$, be a uniform time step. We use the first-order implicit Euler method for the time discretization of the coupled system (19) in the time interval $\left(t^n,t^{n+1}\right)$. An implicit handling of the curvature term (12) is needed to obtain unconditional stability and however, it is too complicated as well. Thus, as in Reference 68, we use a semiimplicit approximation of the curvature

$$\begin{aligned}-\frac{1}{\mathrm{We}}\int_{\Gamma_F^{n+1}}\mathbb{P}_{\mathbf{v}_F^{n+1}}:\left(\nabla_{\Gamma_{\mathbf{v}_F}}\mathbf{v}_h\right)\,d\gamma_F &= -\frac{1}{\mathrm{We}}\int_{\Gamma_F^n}\left[\mathbb{P}_{\mathbf{v}_F^n}+\delta t\nabla_{\Gamma_{\mathbf{v}_F}}\mathbf{u}_h^{n+1}\right]:\left(\nabla_{\Gamma_{\mathbf{v}_F}}\mathbf{v}_h\right)\,d\gamma_F\\ &= -\frac{1}{\mathrm{We}}\int_{\Gamma_F^n}\mathbb{P}_{\mathbf{v}_F^n}:\left(\nabla_{\Gamma_{\mathbf{v}_F}}\mathbf{v}_h\right)\,d\gamma_F-\frac{\delta t}{\mathrm{We}}\int_{\Gamma_F^n}\left(\nabla_{\Gamma_{\mathbf{v}_F}}\mathbf{u}_h^{n+1}\right):\left(\nabla_{\Gamma_{\mathbf{v}_F}}\mathbf{v}_h\right)\,d\gamma_F.\end{aligned}$$

The first term in the above equation is an explicit term and it stays on the right-hand side of the weak formulation, whereas the second term is an implicit term and it goes to the left-hand side. Note that the implicit term is symmetric and positive semidefinite and thus it improves the stability of the discrete system compared with a fully explicit approach.

3.5 | Linearization and mesh movement

In each time step (t^n,t^{n+1}), the nonlinear terms in (19) are handled by an iteration of fixed point type. Let $\mathbf{u}_{h,0}^{n+1}=\mathbf{u}_h^n$, $\boldsymbol{\tau}_{p,h,0}^{n+1}=\boldsymbol{\tau}_{p,h}^n$, and $\mathbf{w}_{h,0}^{n+1}=\mathbf{w}_h^n$. In computations, we adopt the following linearization strategy:

$$\begin{aligned}a\left(\mathbf{u}_h^{n+1}-\mathbf{w}_h^{n+1};\mathbf{u}_h^{n+1},\mathbf{v}_h\right)&\approx a\left(\mathbf{u}_{h,m-1}^{n+1}-\mathbf{w}_{h,m-1}^{n+1};\mathbf{u}_{h,m}^{n+1},\mathbf{v}_h\right),\\ d\left(\mathbf{u}_h^{n+1}-\mathbf{w}_h^{n+1};\boldsymbol{\tau}_{p,h}^{n+1},\boldsymbol{\psi}_h\right)&\approx d\left(\mathbf{u}_{h,m-1}^{n+1}-\mathbf{w}_{h,m-1}^{n+1};\boldsymbol{\tau}_{p,h,m}^{n+1},\boldsymbol{\psi}_h\right)+d\left(\mathbf{u}_{h,m}^{n+1};\boldsymbol{\tau}_{p,h,m-1}^{n+1},\boldsymbol{\psi}_h\right)-d\left(\mathbf{u}_{h,m-1}^{n+1};\boldsymbol{\tau}_{p,h,m-1}^{n+1},\boldsymbol{\psi}_h\right),\\ e\left(\boldsymbol{\tau}_{p,h}^{n+1};\boldsymbol{\tau}_{p,h}^{n+1},\boldsymbol{\psi}_h\right)&\approx e\left(\boldsymbol{\tau}_{p,h,m-1}^{n+1};\boldsymbol{\tau}_{p,h,m}^{n+1},\boldsymbol{\psi}_h\right),\end{aligned}$$

where, $m=1,2,\ldots,\mathrm{M}$, with M being the maximum allowed number of nonlinear iterations. The linearized system of algebraic equations are solved using the multifrontal massively parallel sparse direct solver.[69,70] In computations, the nonlinear iterations are continued until the residual of the monolithic system (19) becomes less than the threshold value of 10^{-7}.

For the mesh movement, we use the linear elastic mesh update technique. Let $\mathbf{Z}_k^n$ be the vertices on the boundary $\partial\Phi_k^n$. We first advect the boundary vertices using the computed flow velocity as follows:

$$\mathbf{Z}_k^{n+1}=\mathbf{Z}_k^n+\delta t\ \mathbf{u}_k^{n+1}.$$

Then, based on the displacement of the boundary vertices $\mathbf{d}_k^{n+1}=\mathbf{Z}_k^{n+1}-\mathbf{Z}_k^n$, the inner points are displaced in a prescribed way to preserve the mesh quality in each domain separately. The displacement $\boldsymbol{\Psi}_k^{n+1}$ of the inner mesh points in both the phases are obtained by solving the following linear elasticity problem with the displacement of boundary vertices as a Dirichlet boundary condition, that is,

Find $\boldsymbol{\Psi}_k^{n+1}\in \mathrm{H}^1\left(\Phi_k^n\right)$, such that

$$\begin{aligned}\nabla\cdot\mathbb{S}(\boldsymbol{\Psi}_k^{n+1})&=0 \qquad \text{in } \Phi_k^n,\\ \boldsymbol{\Psi}_k^{n+1}&=\mathbf{d}_k^{n+1}\quad \text{on } \partial\Phi_k^n,\end{aligned}\tag{21}$$

for k = 1,2, where $\mathbb{S}(\boldsymbol{\Psi}) = \lambda_{L1}(\nabla \cdot \boldsymbol{\Psi})\mathbb{I} + 2\lambda_{L2}\mathbb{D}(\boldsymbol{\Psi})$. Herein, λ_{L1} and λ_{L2} are Lame constants, and in computations we use $\lambda_{L1} = \lambda_{L2} = 1$. Continuous piecewise linear P_1 elements on the same triangular mesh as for solving the flow equations are used for the solution of (21). Once the displacement vector $\boldsymbol{\Psi}_k^{n+1}$ is known for each phase, the mesh velocity is then computed as $\mathbf{w}_k^{n+1} = \boldsymbol{\Psi}_k^{n+1}/\delta t$.

Even though the elastic mesh update technique is used to preserve the mesh quality, the quality of the mesh becomes poor after several time steps due to large deformation in each subdomain. In such an instant, we need to remesh the domain. We have implemented an automatic remeshing algorithm to remesh the domain when the minimum angle of any triangular cell in the mesh is less than 15°. During remeshing, the points on the interface are equally redistributed and a new mesh is generated using the mesh generator triangle.[59,60] The solutions are then interpolated from the old to the newly generated mesh. Furthermore, to minimize the interpolation error, we solve the monolithic system (19) with the interpolated values as initial guess and $\mathbf{w} = 0$ before moving to the next time step. The proposed numerical scheme for the simulation of viscoelastic two-phase flows is implemented in our in-house finite element code ParMooN.[71]

4 | NUMERICAL RESULTS

In this section, we present the numerical results of 3D-axisymmetric buoyancy driven viscoelastic two-phase flows using the proposed numerical scheme. In order to validate the numerical scheme, computations are performed with 2D planar configuration for buoyancy driven Newtonian drop rising in a Newtonian fluid column and compared with the benchmark results.[56] We simultaneously perform a grid independence test for the benchmark configuration. Furthermore, we had validated the numerical scheme in our previous study[55] by comparison of the computational results for a buoyancy driven 2D planar Newtonian drop rising in a Giesekus fluid column with the results of Vahabi and Kamakari.[10] Next, we present a detailed numerical investigation for a buoyancy driven Newtonian drop rising in a viscoelastic fluid column. We examine the effects of viscosity ratio (ε), Newtonian solvent ratio (β), Giesekus mobility factor (α), and Eötvös number (Eo) on the flow dynamics of the rising drop. Furthermore, we also investigate the flow dynamics of a viscoelastic drop rising in a Newtonian fluid column. Key flow features are explained using the visualization of viscoelastic stress profiles. Furthermore, to assist in describing the temporal evolution of the rising drop dynamics quantitatively, we use the following metrics: drop shape, diameter of drop at the axis of symmetry ($D|_{r=0}$), sphericity, kinetic energy, elastic energy, center of mass (z coordinate), and rise velocity. Let $|\Omega_1(t)| := 2\pi\int_{\Phi_1(t)} r\,dr\,dz$ be the volume of the drop. The sphericity of the drop is given by

$$\text{Sphericity} = \frac{\text{Surface area of the volume equivalent sphere}}{\text{Surface area of the drop}} = \frac{A_e}{A}.$$

The surface area of volume-equivalent sphere and surface area of the drop are calculated as follows:

$$A_e = 4\pi\left(\frac{3}{4\pi}|\Omega_1(t)|\right)^{2/3}, \qquad A = 2\pi\int_{\partial\Phi_1(t)} r\,dl.$$

For a perfectly spherical drop, the sphericity will be one and for any other deformed drop it will be less than one. It is a good quantitative measure of the drop deformation. The kinetic and elastic energies of the drop are computed as follows:

$$E_{\text{kinetic}} = \frac{2\pi}{|\Omega_1(t)|}\int_{\Phi_1(t)} (\mathbf{u}\cdot\mathbf{u})\ r\,dr\,dz, \qquad E_{\text{elastic}} = \frac{2\pi}{|\Omega_1(t)|}\int_{\Phi_1(t)} tr(\boldsymbol{\tau}_p)\ r\,dr\,dz.$$

Furthermore, the rise velocity and center of mass (z coordinate) of the drop are given by:

$$\text{Rise velocity} = \frac{2\pi}{|\Omega_1(t)|}\int_{\Phi_1(t)} u_z\ r\,dr\,dz, \qquad \text{Center of mass} = \frac{2\pi}{|\Omega_1(t)|}\int_{\Phi_1(t)} z\ r\,dr\,dz.$$

4.1 | Grid independence test and validation

In this section, we first perform a grid independence test for the proposed numerical scheme and then validate the numerical results using benchmark solutions[56] of a 2D planar rising drop. We consider a Newtonian drop rising in a Newtonian fluid column with the following benchmark parameters (refer test case-1 in table 1 of Reference 56): $\rho_1 = 100$, $\rho_2 = 1000$, $\mu_{0,1} = 1$, $\mu_{0,2} = 10$, $g = 0.98$, $\sigma = 24.5$, $D = 0.5$, and $h_c = 2.0$. Using the characteristic length L = 1 and characteristic velocity $U_\infty = \sqrt{Lg}$, we get the following dimensionless quantities $Re_2 = 99$, $Eo = 40$, $\rho_1/\rho_2 = 0.1$, $\epsilon = 10$, $\beta_1 = 1$, and $\beta_2 = 1$. In order to identify a grid that provides a grid-independent solution, we consider five different meshes of varying mesh sizes. In particular, we vary the number of degrees of freedom (DOFs) on the interface. The characteristics of these meshes are tabulated in Table 1 . The time-step length is set as $\delta t = 0.0005$ and the computations are performed till I = 3.0.

Figure 3 depicts the convergence behavior of the temporal evolution of circularity, rise velocity, and center of mass of the rising bubble with different meshes. From the zoomed plots (refer Figure 3D-F), we can observe that the considered flow variables gradually tend to a grid-independent value when the mesh becomes finer. In particular, the numerical results obtained with the mesh L4 is quite close to those obtained with the mesh L5, which shows the grid independence of the numerical solution. In order to have a fine balance between the computational cost and the accuracy, all numerical

TABLE 1 Grid independence test: characteristics of triangular meshes

Mesh	DOFs on Γ_F	h_0	Cells	Total DOFs
L1	100	0.015705380	1837	16 793
L2	200	0.007853659	2576	23 454
L3	400	0.003926950	3767	34 183
L4	600	0.002617982	4980	45 094
L5	800	0.001963490	6237	56 425

Abbreviation: DOFs, degrees of freedom.

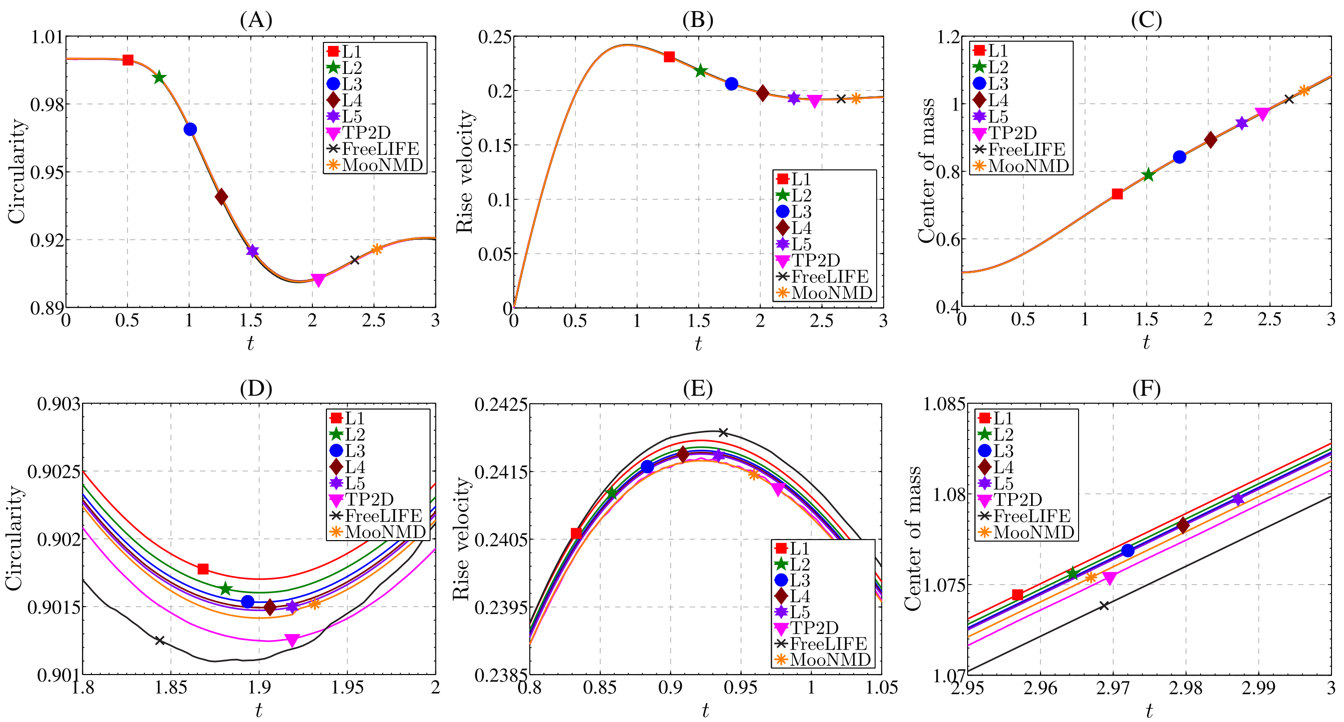

FIGURE 3 Grid independence test and validation: temporal evolution of circularity (A), (D), rise velocity (B), (E), and center of mass (C), (F) of a Newtonian drop rising in a Newtonian fluid column using five different meshes compared with benchmark solutions[56] [Color figure can be viewed at wileyonlinelibrary.com]

TABLE 2 Newtonian drop rising in a Newtonian fluid column: Comparison of results with the benchmark solutions in the literature[56]

Metric/Reference	L5 (Current Work)	TP2D[56]	FreeLIFE[56]	MooNMD[56]
min(Circularity)	0.9015	0.9013	0.9011	0.9013
$t\|_{\text{min(Circularity)}}$	1.9005	1.9041	1.8750	1.9000
max(Rise velocity)	0.2418	0.2417	0.2421	0.2417
$t\|_{\text{max(Rise velocity)}}$	0.9214	0.9213	0.9313	0.9239
Center of mass at $t = 3.0$	1.0822	1.0813	1.0799	1.0817

TABLE 3 Time-step convergence test for a Newtonian drop rising in a Newtonian fluid column

Metric/Time Step	0.002	0.001	0.0005	0.00025
min(Circularity)	0.9022	0.9017	0.9015	0.9015
$t\|_{\text{min(Circularity)}}$	1.8980	1.8996	1.9005	1.9007
max(Rise velocity)	0.2415	0.2417	0.2418	0.2418
$t\|_{\text{max(Rise velocity)}}$	0.9225	0.9218	0.9214	0.9213
Center of mass at $t = 3.0$	1.0830	1.0825	1.0822	1.0822

results in the following sections are obtained with the mesh L4. Note that we have presented the grid independence test for a 2D Planar configuration. However, the same convergence behavior is also observed with L4 and L5 meshes in 3D-axisymmetric configuration. Furthermore, the benchmark solutions are also plotted in Figure 3 and our results agree well with the benchmark results. In order to quantitatively compare our numerical solutions with the benchmark results, the minimum circularity, time at minimum circularity, maximum rise velocity, time at maximum rise velocity, and center of mass at $t = 3.0$ are tabulated in Table 2. We can observe that our results agree well with those in the literature.[56] Since it is a moving domain problem, we need to choose a smaller time step to capture the physics (the dynamics of moving interface) though the implicit time discretization allows larger time step. Moreover, we performed a time-step convergence and the results for different time-step lengths 0.002, 0.001, 0.0005, and 0.00025 with L4 mesh are tabulated in Table 3. We can observe that the numerical values with time-step lengths 0.0005 and 0.00025 converge to a time-step independent value. Furthermore, for the order of convergence of the proposed LPS scheme for computations of viscoelastic fluid flows, we refer to our previous study.[54] Using the method of manufactured solutions we observed that if r is the polynomial order of the finite element basis function, then the optimal order of convergence for the velocity and pressure in L^2-norm is of the order $r + 1$, whereas the optimal order of convergence for the viscoelastic conformation stress in L^2-norm is expected to be $r + 1/2$.

4.2 | Newtonian drop rising in a viscoelastic fluid column

In this section, we consider a 3D-axisymmetric Newtonian drop rising in a viscoelastic fluid column due to buoyancy. We designate a base case to systematically examine the effects of various flow parameters. The base case is defined as: $\mathrm{Re}_2 = 10$, $\mathrm{Eo} = 400$, $\mathrm{Wi}_2 = 25$, $\rho_1/\rho_2 = 0.1$, $\varepsilon = 10$, $\beta_1 = 1.0$, $\beta_2 = 0.75$, $\alpha_2 = 0.1$, $D = 0.5$, and $h_c = 2.0$. The computational domain is triangulated into an interface-resolved mesh using the mesh generator Triangle[59,60] based on constrained Delaunay triangulation. We limit the maximum nondimensional area of each cell in the mesh to 0.001 during the triangulation (initially and as well as during the remeshing). This results in 1835 and 3111 cells in the initial inner and outer domains, respectively. The finite element spaces used in computations for the velocity/pressure/viscoelastic stress are P_2^{bubble} / P_1^{disc} / P_2^{bubble}. This choice of initial mesh and finite element spaces results in 49742 velocity, 14838 pressure, and 74613 viscoelastic DOFs. Furthermore, we use a constant time step $\delta t = 0.0005$ and 600 DOFs on the interface with $h_0 = 0.002617982$, where h_0 is the mesh size at $t = 0$. In computations, the number of cells and the number of DOFs might change during the remeshing. Furthermore, the stabilization constants used in computations are $c_1 = 0.005$, $c_2 = 0.005$, and $c_3 = 0.005$. In order to avoid the effect of the presence of the wall at the top of the domain, simulations were stopped when the drop reaches a constant velocity or when its velocity begins to decrease due to the proximity of the top surface.

Figure 4 presents the viscoelastic stress profiles for the base case flow parameters at dimensionless time instances $t = 1.0, 4.0, 6.0$, and 9.0. At time $t = 0$, the drop is of a spherical shape with initial velocities of the drop and the bulk fluid column assumed to be zero and the viscoelastic conformation stress tensor is set as $\boldsymbol{\tau}_{p,0} = \mathbb{I}$. Initially, the buoyancy force generated by the density difference between two fluids accelerates the drop in the opposite direction of the gravity, that is, the drop rises up in the bulk fluid column. The transient behavior of a buoyant drop accelerating from rest in a viscoelastic fluid column depends on its volume and the magnitudes of the viscous and viscoelastic stresses, which themselves depend on the fluid properties such as the viscosity and the relaxation time. The drop is driven by the force of buoyancy, while the viscous and viscoelastic stresses resist its motion. If the deforming stresses at the interface are sufficiently smaller than the interfacial tension force, the drop shape remains approximately spherical. However, when these deforming stresses are significant the interface deforms and the drop shape changes depending on the properties of the bulk fluid: it deforms to an oblate shape in inertia-dominated flows and to a prolate shape with or without a cusp-like trailing end in flows, in which viscoelasticity is important.

At $t = 1.0$, we can observe that the maximum values of viscoelastic stress component τ_{rr} starts to accumulate at the front stagnation point, while τ_{rz} gets built up along the entire circumference of the bubble. However, the maximum values of τ_{zz} are concentrated at the rear stagnation point. The initial motion of the drop is dominated by viscous stresses as the viscoelastic stresses take some time to build up. Furthermore, along the interface, the interfacial tension force dominates compared with the viscous and viscoelastic stresses. Hence, the shape of the drop is more spherical at $t = 1.0$, similar to a Newtonian drop rising in a Newtonian fluid column. At $t = 4.0$, we can observe that the peak magnitude of viscoelastic stresses have increased, but still the viscous stresses continue to dominate the flow dynamics and hence, the drop shape remains more spherical.

At time $t = 6.0$, the drop starts to become prolate and this is an indication that the viscoelastic stresses are starting to dominate the flow dynamics. In particular, the viscous and viscoelastic stresses overcome the interfacial tension. Furthermore, the maximum values of τ_{zz} and minimum values of τ_{rr} are concentrated at the rear stagnation point. Hence, the polymers near the trailing end of the drop get stretched along the z direction. The extensional viscoelastic stresses in general being large in a thin section at the trailing end of the drop can surmount the interfacial tension, hence forming a cusp-like trailing end. The cusp-like trailing end becomes more and more obvious as the time progresses. Since, the maximum values of τ_{rr} and minimum values of τ_{zz} occur at the front stagnation point, the upstream axial flow experiences a strong turn tangential to the drop surface so that the polymers are greatly extended in the radial directions. Thus, the drop does not experience noticeable deformation in the vicinity of its front end. With further advancement in time, the viscoelastic stresses completely dominate the rising drop dynamics. At $t = 9.0$, τ_{zz} gets concentrated only in the rear stagnation point resulting in the trailing end of the drop being extremely pulled out. Next, we perform a parametric study to examine the effects of viscosity ratio, Newtonian solvent ratio, Giesekus mobility factor, and Eötvös number on the rising drop dynamics in a viscoelastic fluid column.

4.2.1 | Influence of viscosity ratio on the drop dynamics

To study the influence of viscosity ratio on the rising drop dynamics, we consider the base case flow parameters and vary only the viscosity ratio. In particular, we vary only the total viscosity of the inner phase and keep all other parameters the same. The following five different viscosity ratios are used in this study: (i) $\epsilon = 1$, (ii) $\epsilon = 2$, (iii) $\epsilon = 3$, (iv) $\epsilon = 5$, and (v) $\epsilon = 10$. Figure 5 presents the computational results for all the five variants of viscosity ratios. By increasing the viscosity ratio, in principle we only increase the Reynolds number of the drop while other parameters remain the same. Hence, with an increase in the Reynolds number of the drop, it forces the drop to rise with a higher velocity and the same can be observed in Figure 5F. Initially, the motion is inertia dominated due to buoyancy and hence, the rise velocity increases tremendously till about $t = 0.3$. After that, the viscous and viscoelastic stresses resist the buoyant force and we can observe an upward movement of the drop with a steady rise velocity. The kinetic energy of the drop increases with an increase in the viscosity ratio, since it is accompanied by an increase in the rise velocity. We can observe from Figure 5D, that after the initial acceleration the temporal evolution of the kinetic energy of the drop curves seem to be parallel with an increase in the viscosity ratio. Furthermore, the drop also rises higher with increased rise velocity and kinetic energy in the drop and thus, the center of mass of the drop is higher with an increase in the viscosity ratio, see Figure 5E.

Figure 5A depicts the drop shapes at $t = 9$. For high viscosity ratios, the drop surface close to the trailing end becomes concave and a very long and narrow tail develops. This is due to the fact that, with an increase in the Reynolds number of the drop, there is increased generation and accumulation of extensional viscoelastic stresses at the rear stagnation point.

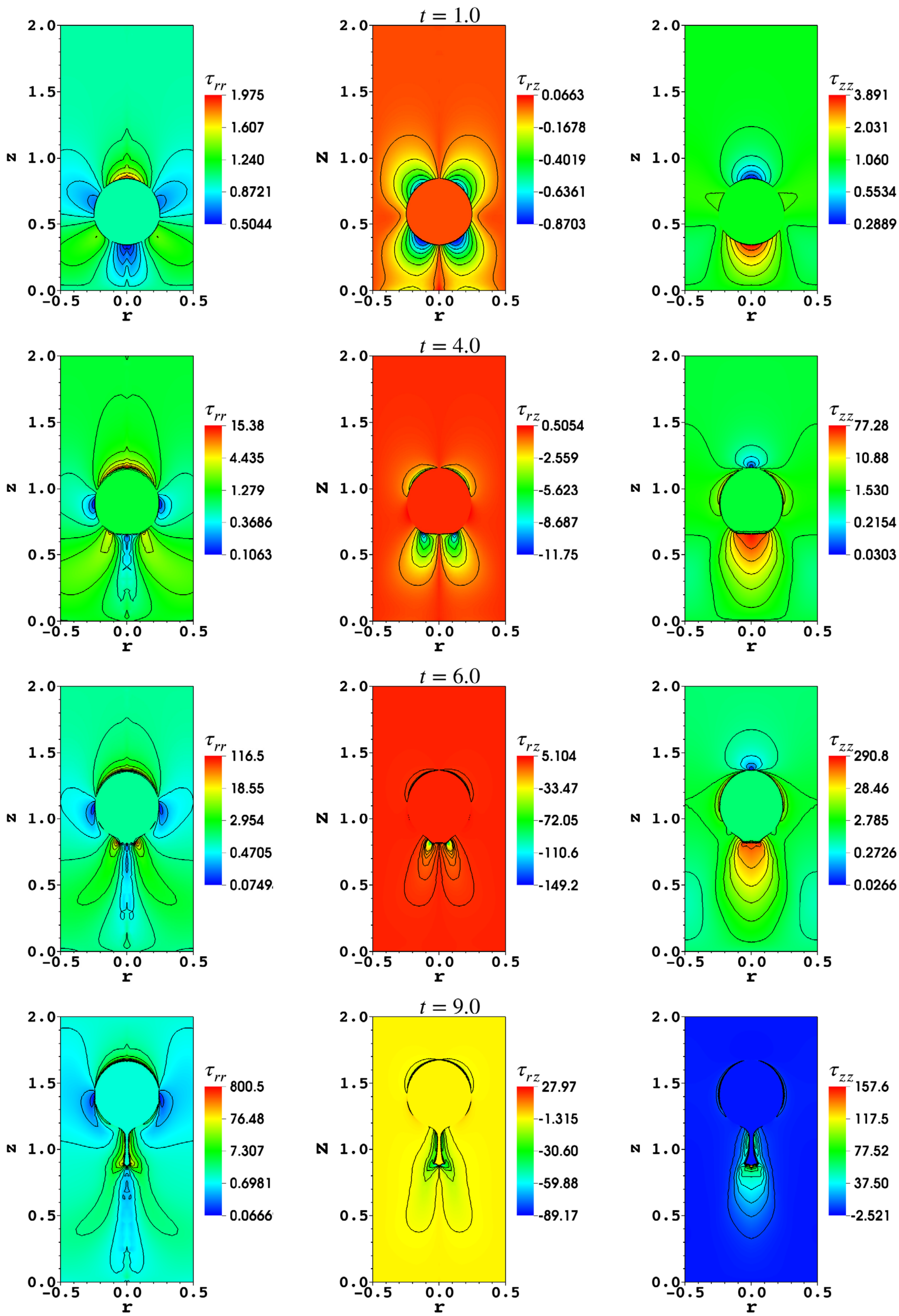

FIGURE 4 Viscoelastic conformation stress profiles for a Newtonian drop rising in a viscoelastic fluid column with flow parameters $\mathrm{Re}_2 = 10$, $\mathrm{Eo} = 400$, $\mathrm{Wi}_2 = 25$, $\rho_1/\rho_2 = 0.1$, $\varepsilon = 10$, $\beta_1 = 1.0$, $\beta_2 = 0.75$, $\alpha_2 = 0.1$, $D = 0.5$, and $h_c = 2.0$ at dimensionless times $t = 1.0$, 4.0, 6.0, and 9.0 [Color figure can be viewed at wileyonlinelibrary.com]

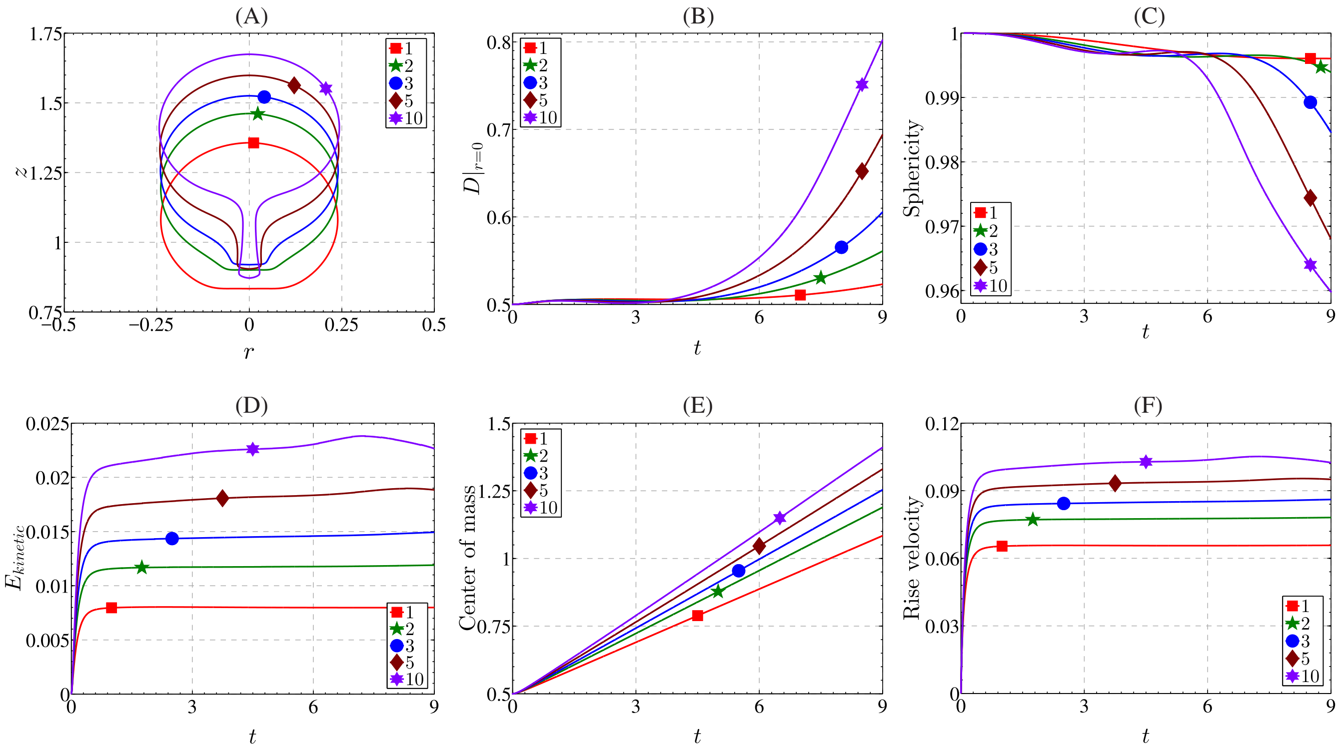

FIGURE 5 Influence of viscosity ratio for a Newtonian drop rising in a viscoelastic fluid column: (A) drop shape at $t = 9$, (B) diameter of the drop at $r = 0$, (C) sphericity, (D) kinetic energy, (E) center of mass, and (F) rise velocity of the drop for different viscosity ratios (i) $\epsilon = 1$, (ii) $\epsilon = 2$, (iii) $\epsilon = 3$, (iv) $\epsilon = 5$, and (v) $\epsilon = 10$ with flow parameters $\mathrm{Re}_2 = 10$, $\mathrm{Eo} = 400$, $\mathrm{Wi}_2 = 25$, $\rho_1/\rho_2 = 0.1$, $\beta_1 = 1.0$, $\beta_2 = 0.75$, $\alpha_2 = 0.1$, $D = 0.5$, and $h_c = 2.0$ [Color figure can be viewed at wileyonlinelibrary.com]

Hence, at a given time the drop with higher viscosity ratio will show greater extended trailing edge characteristics in the drop and the same in observed in Figure 5A. However, for low viscosity ratios, the drop does have an extended trailing edge, but occurs at a later time as the viscoelastic stresses are accumulated slowly. Furthermore, Figure 5B presents the temporal evolution of the diameter of the drop at the axis of symmetry. We can observe that till around $t = 4$, the drop rises with almost the same diameter, which indicates that the interfacial tension dominated over the viscous and viscoelastic stresses till $t = 4$. However, after $t = 4$, the diameter of the drop increases with an increase in the viscosity ratio, as viscoelastic stresses start to dominate the drop shapes. Furthermore, Figure 5C depicts the temporal evolution of the sphericity of the drop. It is a good indicative of the drop deformation. As expected, we can observe that the sphericity of the drop at $t = 9$ decreases with an increase in the viscosity ratio.

The drop rising in a viscoelastic fluid column reveals an interesting flow phenomenon such that in the wake of the rising drop, the velocity field very close to the trailing end is in the direction of the motion of the drop, whereas it reverses its direction at a small distance away from the trailing end, which is commonly referred to as negative wake.[72] In the case of Newtonian fluids, the fluid velocity behind the drop is always in the same direction as the drop's motion. Figure 6 depicts the negative wake phenomenon. At $t = 13.25$, the fluid velocity behind the drop is in the same direction as the drop's motion. However, immediately after $t = 13.25$ the flow direction starts to reverse in the wake region and at $t = 16.0$, we can observe that the flow direction has completely reversed at a small distance away from the trailing end.

4.2.2 | Influence of Newtonian solvent ratio on the drop dynamics

In this section, we study the influence of Newtonian solvent ratio on the rising Newtonian drop dynamics in a viscoelastic fluid column. We consider the base case flow parameters and vary only the Newtonian solvent ratio of the bulk fluid column. In particular, we vary the Newtonian solvent viscosity and polymeric viscosity of the bulk fluid, but keep the total viscosity constant. Four different values are used for the Newtonian solvent ratio in this study, which are as follows:

(i) $\beta_2 = 0.625$, (ii) $\beta_2 = 0.75$, (iii) $\beta_2 = 0.875$, and (iv) $\beta_2 = 1.0$. Lower the Newtonian solvent ratio, greater is the polymeric viscosity and lesser is the Newtonian viscosity, thereby increasing the viscoelastic character of the fluid column. Figure 7 presents the numerical results for different Newtonian solvent ratios. Note that the case $\beta_2 = 1.0$ represents a Newtonian drop rising in a Newtonian fluid column. From Figure 7A, we can observe that the drop shape at the trailing end develops a longer and narrower tail and also rises higher with decrease in the Newtonian solvent ratio. With increased viscoelasticity in the bulk fluid, the extensional stresses at the rear stagnation point increases leading to a longer and narrower tail. The greater rise in the drop is accompanied by a higher center of mass, see Figure 7E. Furthermore, the kinetic energy and the rise velocity of the drop increases with a decrease in the Newtonian solvent ratio, refer Figure 7E,F.

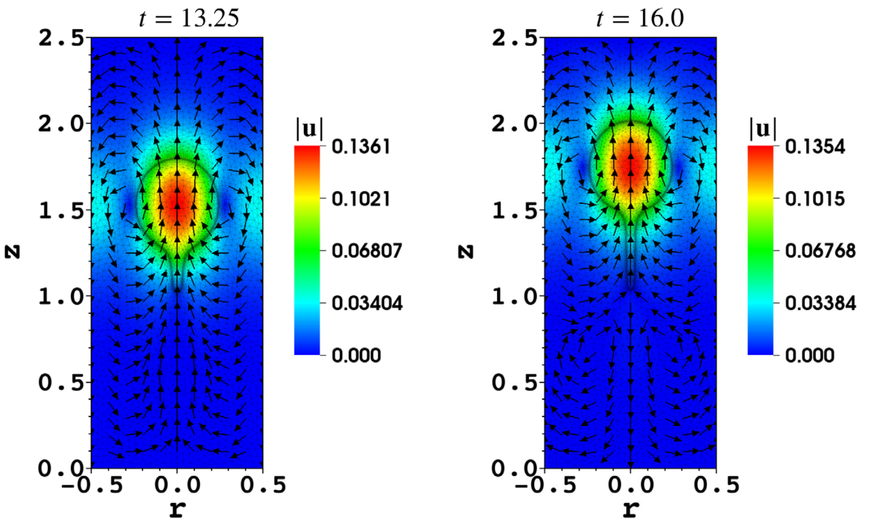

FIGURE 6 Magnitude of velocity profiles and velocity vectors at dimensionless times $t = 13.25$ and 16.0 for a Newtonian bubble rising in a viscoelastic fluid column with flow parameters: $\mathrm{Re}_2 = 10$, $\mathrm{Eo} = 400$, $\mathrm{Wi}_2 = 25$, $\varepsilon = 2$, $\rho_1/\rho_2 = 0.1$, $\beta_1 = 1.0$, $\beta_2 = 0.75$, $\alpha_2 = 0.1$, $D = 0.5$, and $h_c = 2.5$ [Color figure can be viewed at wileyonlinelibrary.com]

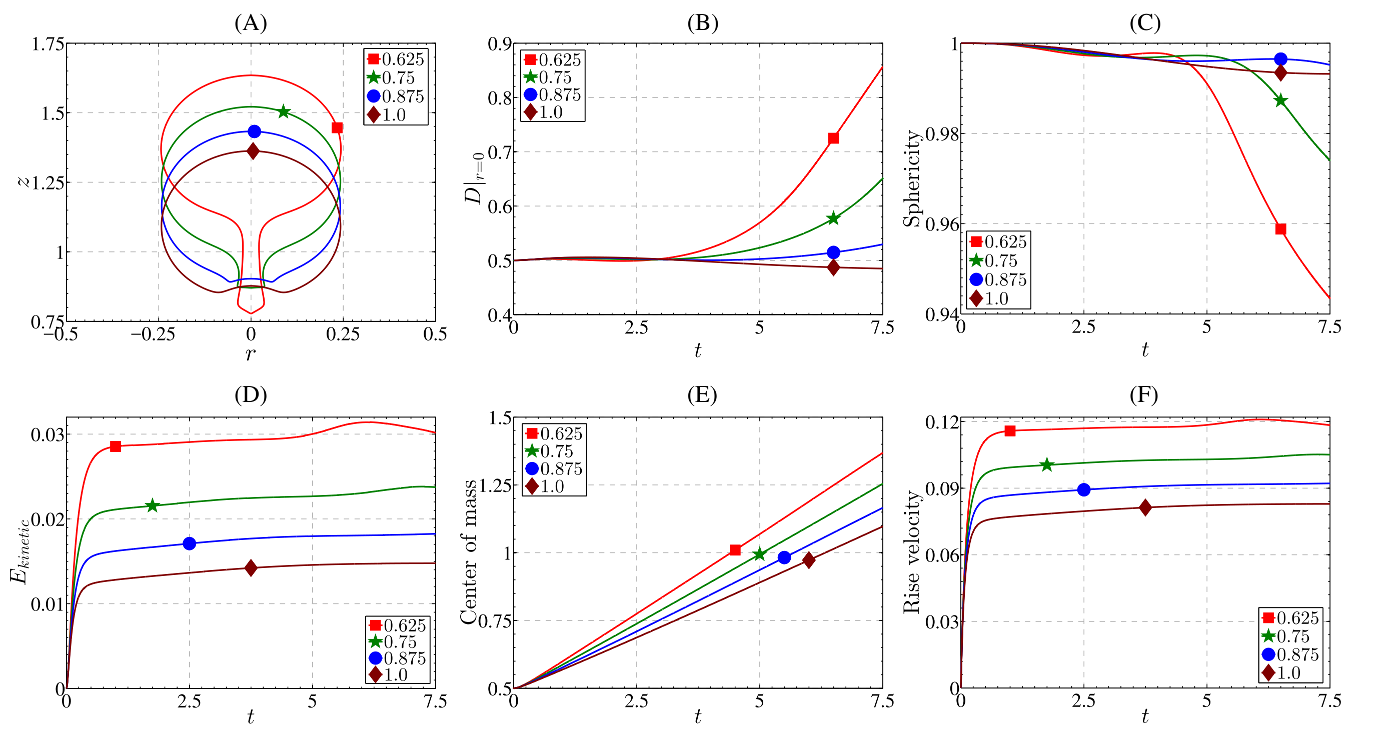

FIGURE 7 Influence of Newtonian solvent ratio for a Newtonian drop rising in a viscoelastic fluid column: (A) drop shape at $t = 7.5$, (B) diameter of the drop at $r = 0$, (C) sphericity, (D) kinetic energy, (E) center of mass, and (F) rise velocity of the drop for different Newtonian solvent ratios (i) $\beta_2 = 0.625$, (ii) $\beta_2 = 0.75$, (iii) $\beta_2 = 0.875$, and (iv) $\beta_2 = 1.0$ with flow parameters $\mathrm{Re}_2 = 10$, $\mathrm{Eo} = 400$, $\mathrm{Wi}_2 = 25$, $\varepsilon = 10$, $\rho_1/\rho_2 = 0.1$, $\beta_1 = 1.0$, $\alpha_2 = 0.1$, $D = 0.5$, and $h_c = 2.0$ [Color figure can be viewed at wileyonlinelibrary.com]

The curves become parallel after the viscous and viscoelastic stresses start to overcome the interfacial tension. In Figure 7B, we can observe that the diameter of the drop at the axis of symmetry increases to a greater extent with a decrease in the Newtonian solvent ratio. This occurs since with an increase in the viscoelastic character of the outer fluid column, the drop develops a longer trailing edge due to greater extensional viscoelastic stresses near the rear stagnation point. Furthermore, the sphericity of the drop decreases to a greater extent with a decrease in the Newtonian solvent ratio due to increased deformation at the rear end, see Figure 7C.

4.2.3 | Influence of Giesekus mobility factor on the drop dynamics

To examine the influence of Giesekus mobility factor on the Newtonian drop rising in a viscoelastic fluid column, we consider the following five different Giesekus factors: (i) $\alpha_2 = 0.1$, (ii) $\alpha_2 = 0.2$, (iii) $\alpha_2 = 0.5$, (iv) $\alpha_2 = 0.75$, and (v) $\alpha_2 = 1.0$. The other flow parameters are the same as the base case. Figure 8 presents the computational results for different Giesekus factors. With an increase in the Giesekus factor, the shear thinning effects increases. Hence, with increased shear thinning, the drop is expected to have higher rise velocity and eventually greater kinetic energy. From Figure 8D,F, we can observe that there is not much visible effect of Giesekus factor. However, from the zoomed plots, we can observe the shear thinning effect very clearly. Increasing the Giesekus factor leads to a decrease in the magnitude of the viscoelastic stresses generated in the bulk fluid column. Hence, from Figure 8A, we can observe that the trailing end of the drop becomes flatter and the tail becomes shorter with an increase in the Giesekus factor. Since the tail becomes shorter, the magnitude of the increase of the diameter of the drop at the axis of symmetry decreases with an increase in the Giesekus factor, see Figure 8B. The sphericity of the drop decreases to a greater extent with a decrease in the Giesekus factor due to large deformation at the tail end of the drop. Furthermore, from Figure 8E, we can observe that the center of the mass of the drop is higher for larger values of Giesekus factor as the tail end of the drop becomes shorter and less extended out.

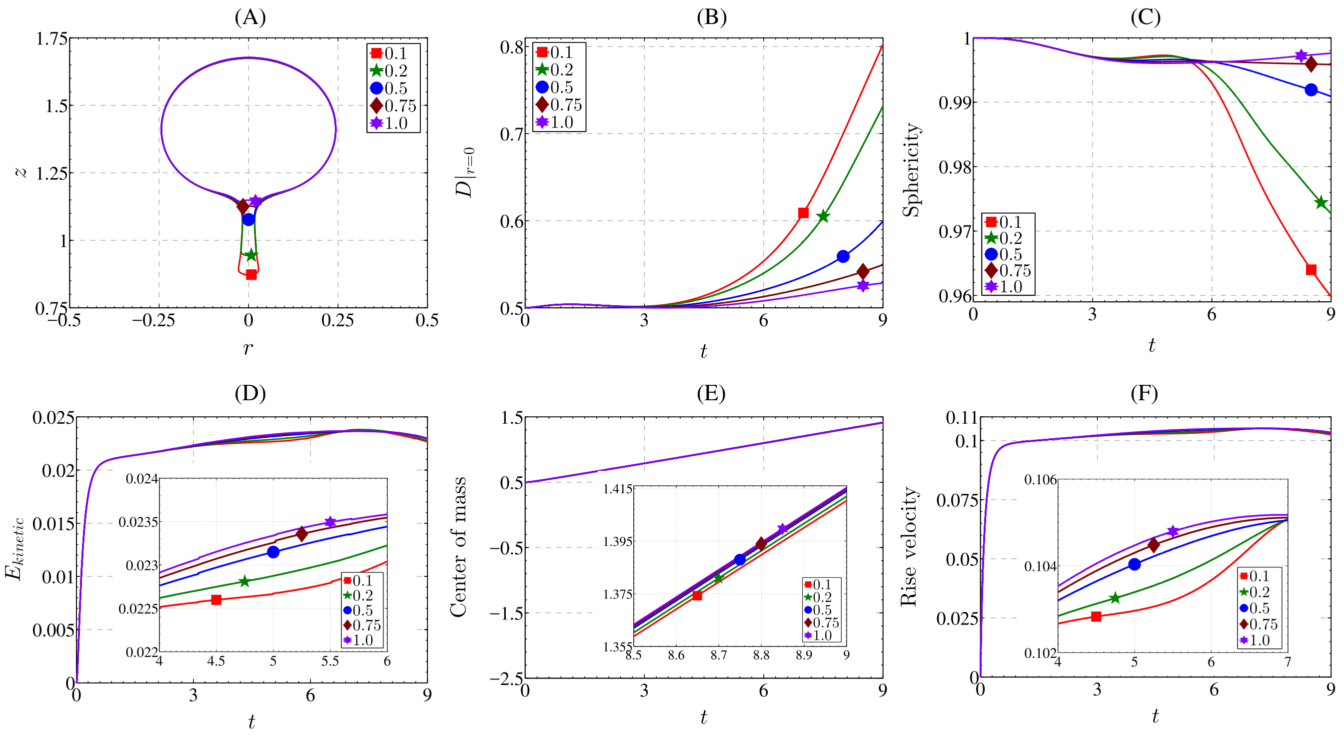

FIGURE 8 Influence of Giesekus mobility factor for a Newtonian drop rising in a viscoelastic fluid column: (A) drop shape at $t = 9$, (B) diameter of the drop at $r = 0$, (C) sphericity, (D) kinetic energy, (E) center of mass, and (F) rise velocity of the drop for different Giesekus mobility factors (i) $\alpha_2 = 0.1$, (ii) $\alpha_2 = 0.2$, (iii) $\alpha_2 = 0.5$, (iv) $\alpha_2 = 0.75$, and (v) $\alpha_2 = 1.0$ with flow parameters $\mathrm{Re}_2 = 10$, $\mathrm{Eo} = 400$, $\mathrm{Wi}_2 = 25$, $\epsilon = 10$, $\rho_1/\rho_2 = 0.1$, $\beta_1 = 1.0$, $\beta_2 = 0.75$, $D = 0.5$, and $h_c = 2.0$ [Color figure can be viewed at wileyonlinelibrary.com]

4.2.4 | Influence of Eötvös number on the drop dynamics

In this section, we study the influence of Eötvös number on the rising Newtonian drop dynamics in a viscoelastic fluid column. We consider the base case flow parameters and vary only the Eötvös number, that is, vary the interfacial tension. Five different values are used for the Eötvös number in this study, which are as follows: (i) Eo = 25, (ii) Eo = 50, (iii) Eo = 100, (iv) Eo = 200, and (v) Eo = 400. Increasing the Eötvös number, decreases the interfacial tension, thereby making the interface more easily deformable and thus increases the degree of interface stretching by the polymer stress. In Figure 9A, we can observe that at low Eötvös numbers, the drop shapes are more similar to a Newtonian drop rising in a Newtonian fluid column. In fact, with further advancement in time, they still do not deform as observed with high Eötvös numbers. This phenomenon can be explained by the fact that there exists a critical capillary number, beyond which the drop experiences unsteady deformations in the form of an extended trialing edge. For interface flows, capillary number is the ratio of Eötvös number to the Reynolds number. Hence, by increasing the Eötvös number, we actually increase the capillary number. From Figure 9A, we can comment that the critical Eötvös number for unsteady drop shapes for the considered flow parameters is between 50 and 100 as drops beyond Eo = 100 become cusp-like shaped.

Since, the extended trailing edge behavior increases with an increase in the Eötvös number, the diameter of the drop at the axis of symmetry increases when the viscoelastic stresses start to overcome the interfacial tension, refer Figure 9B. However, till the motion is inertia dominated, there is not much effect of Eötvös number on the diameter of the drop. Furthermore, Figure 9C presents the temporal evolution of the sphericity of the drop. It quite natural that, with increase in the Eötvös number, the interface becomes more deformable and hence, the sphericity decreases to a greater extent. Next, Figure 9D,F depicts the kinetic energy and rise velocity of the drop. We can observe that they increase to a greater extent with an increase in the Eötvös number. Furthermore, the center of mass of the drop is higher for larger Eötvös numbers, see Figure 9E, as the drop rises higher with greater rise velocity.

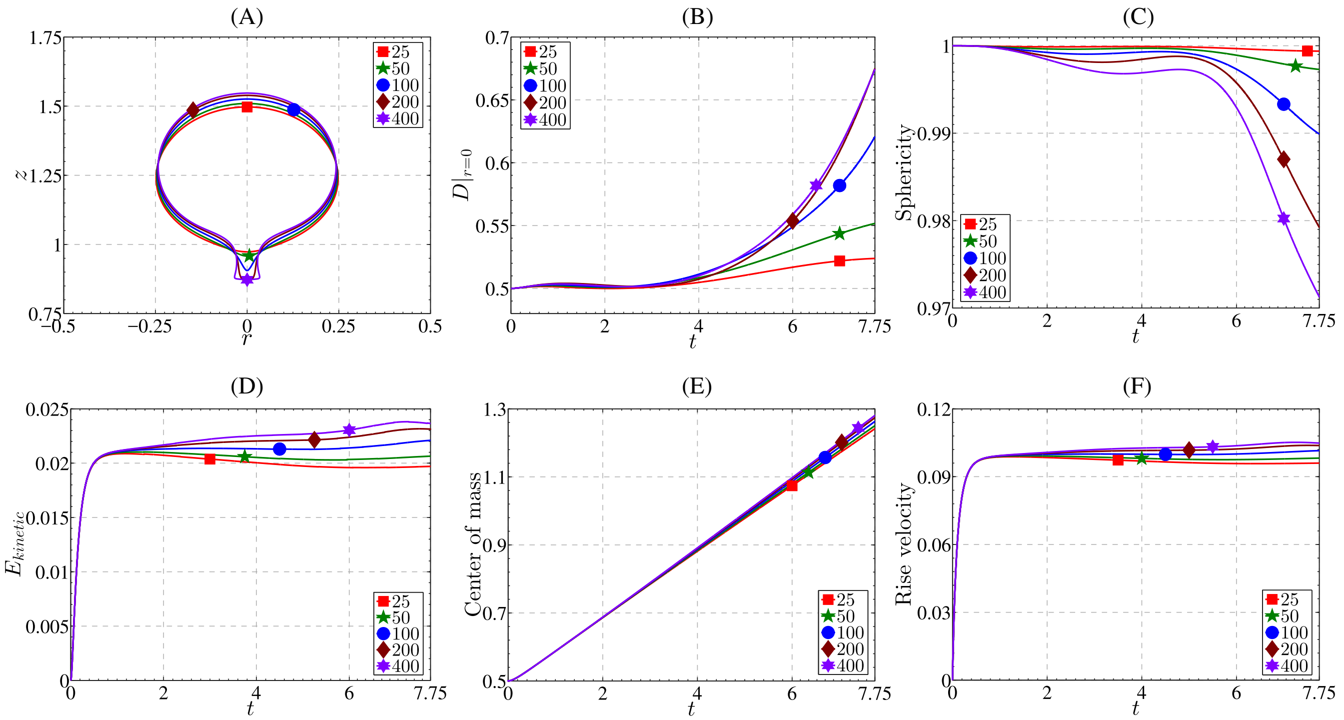

FIGURE 9 Influence of Eötvös number for a Newtonian drop rising in a viscoelastic fluid column: (A) drop shape at $t = 7.75$, (B) diameter of the drop at $r = 0$, (C) sphericity, (D) kinetic energy, (E) center of mass, and (F) rise velocity of the drop for different Eötvös numbers (i) Eo = 25, (ii) Eo = 50, (iii) Eo = 100, (iv) Eo = 200, and (v) Eo = 400 with flow parameters $\mathrm{Re}_2 = 10$, $\mathrm{Wi}_2 = 25$, $\epsilon = 10$, $\rho_1/\rho_2 = 0.1$, $\beta_1 = 1.0$, $\beta_2 = 0.75$, $\alpha_2 = 0.1$, $D = 0.5$, and $h_c = 2.0$ [Color figure can be viewed at wileyonlinelibrary.com]

4.3 | Viscoelastic drop rising in a Newtonian fluid column

In this section, we consider a buoyancy driven 3D-axisymmetric viscoelastic drop rising in a Newtonian fluid column. The base case parameters for studying the effects of various flow variables are defined as follows: $Re_2 = 10$, $Eo = 400$, $Wi_1 = 10$, $\rho_1/\rho_2 = 0.1$, $\epsilon = 2$, $\beta_1 = 0.5$, $\beta_2 = 1.0$, $\alpha_1 = 0.1$, $D = 0.5$, and $h_c = 2.5$. During the triangulation, we limit the maximum area of each cell in the mesh to 0.001, which leads to 1198 and 2954 cells in the initial inner and outer domains, respectively. The finite element spaces used in computations for the velocity/pressure/viscoelastic stress are $P_2^{\text{bubble}}/P_1^{\text{disc}}/P_2^{\text{bubble}}$. This choice of initial mesh and finite element spaces results in 41854 velocity, 12456 pressure, and 62781 viscoelastic DOFs. Furthermore, we use a constant time step $\delta t = 0.0005$ and 400 DOFs on the interface with initial mesh size $h_0 = 0.00392695$. The stabilization constants used in computations are $c_1 = 0.05$, $c_2 = 0.05$, and $c_3 = 0.05$.

Figure 10 presents the viscoelastic stress profiles in the drop for the base case flow parameters at dimensionless time instances $t = 2$, 6, 10, and 20. Initially, the drop is of a spherical shape with $\mathbf{u}_0 = 0$ and $\boldsymbol{\tau}_{p,0} = \mathbb{I}$. The viscoelastic drop rises up in the bulk fluid column due to buoyancy force generated by the density difference between the two immiscible fluids.

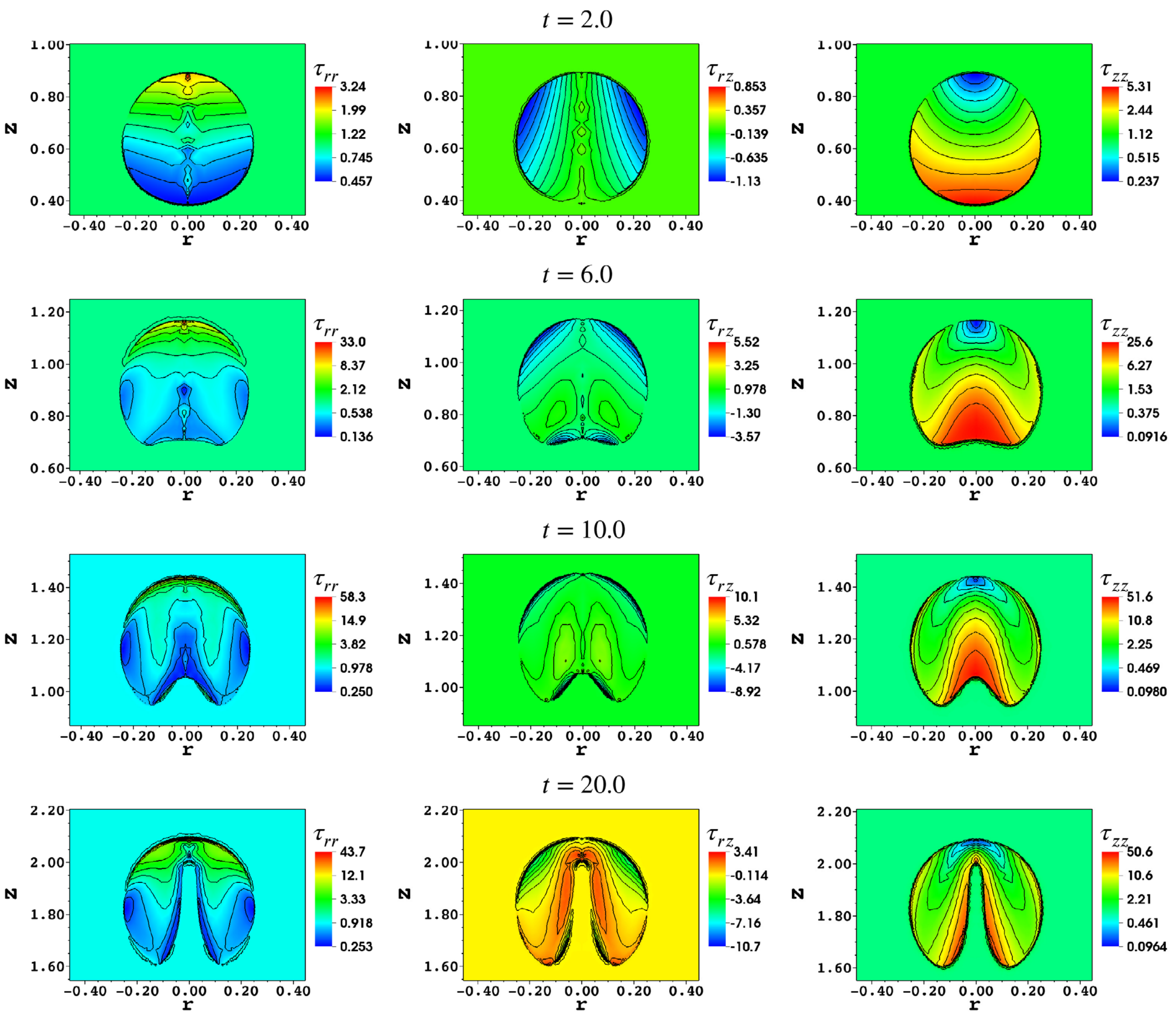

FIGURE 10 Viscoelastic conformation stress profiles for a viscoelastic drop rising in a Newtonian fluid column with flow parameters $Re_2 = 10$, $Eo = 400$, $Wi_1 = 10$, $\rho_1/\rho_2 = 0.1$, $\epsilon = 2$, $\beta_1 = 0.5$, $\beta_2 = 1.0$, $\alpha_1 = 0.1$, $D = 0.5$, and $h_c = 2.5$ at dimensionless times $t = 2$, 6, 10, and 20 [Color figure can be viewed at wileyonlinelibrary.com]

As the drop rises, the initial motion of the drop is inertia dominated as viscoelastic stresses take some time to build up. Thus, at $t = 2$, we can observe that the drop shape is still more spherical. However, at $t = 6$, the drop at the tail end starts to deform and it attains a cylindrical shape with a dimpled trailing end. The viscous and viscoelastic stresses start to overcome the interfacial tension. The maximum values of viscoelastic stress component τ_{rr} are concentrated in the top end of the drop, while τ_{zz} is built up more near the tail end of the drop. The polymers inside the drop is stretched along the flow direction. Since the local flow direction is normal to the interface at the rear stagnation point, the polymer stress component τ_{zz} reaches its maximum value at the tail end of the drop and pulls the interface inward. Since, the maximum values of τ_{rr} and minimum values of τ_{zz} occur at the top end of the drop, the upstream axial flow experiences a strong turn tangential to the drop surface so that the polymers are greatly extended in the radial directions. Thus, the drop does not experience noticeable deformation at its front end. With further advancement in time, the viscoelastic stresses increases and hence the drop at the trailing end is more pulled up inward. The simulations were stopped at $t = 20$, as beyond that the drop shall start to split and the assumption of no topological change in the computational domain shall fail when the drop splits.

4.3.1 | Influence of viscosity ratio on the drop dynamics

In this section, we study the influence of viscosity ratio on the rising viscoelastic drop dynamics. We consider the base case flow parameters and vary only the viscosity ratio. The following five different viscosity ratios are used in this study: (i) $\epsilon = 1.5$, (ii) $\epsilon = 2.0$, (iii) $\epsilon = 2.5$, (iv) $\epsilon = 3.0$, and (v) $\epsilon = 4.0$. Figure 11 presents the numerical results for different viscosity ratios. With an increase in the viscosity ratio, the Reynolds number of the drop increases and it forces the drop to rise with a higher rise velocity and the same can be observed in Figure 11F. Since, the drop rises with a higher velocity, the kinetic energy will also be higher, refer Figure 11D. Figure 11E presents the temporal evolution of elastic energy in the drop. The elastic energy in the drop depends on the viscoelastic stresses in the drop. Since, the viscoelastic stresses

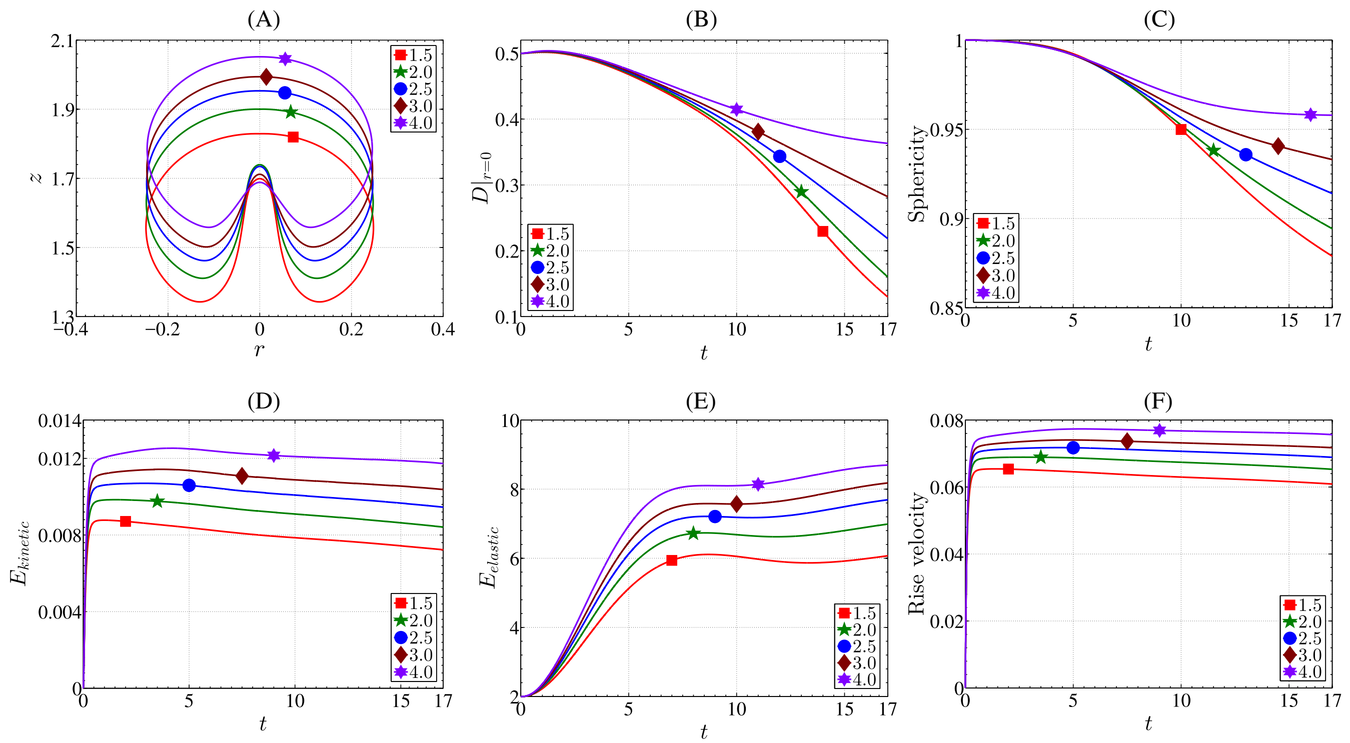

FIGURE 11 Influence of viscosity ratio for a viscoelastic drop rising in a Newtonian fluid column: (A) drop shape at $t = 17$, (B) diameter of the drop at $r = 0$, (C) sphericity, (D) kinetic energy, (E) elastic energy, and (F) rise velocity of the drop for different viscosity ratios (i) $\epsilon = 1.5$, (ii) $\epsilon = 2.0$, (iii) $\epsilon = 2.5$, (iv) $\epsilon = 3.0$, and (v) $\epsilon = 4.0$ with flow parameters $\mathrm{Re}_2 = 10$, $\mathrm{Eo} = 400$, $\mathrm{Wi}_1 = 10$, $\rho_1/\rho_2 = 0.1$, $\beta_1 = 0.5$, $\beta_2 = 1.0$, $\alpha_1 = 0.1$, $D = 0.5$, and $h_c = 2.5$ [Color figure can be viewed at wileyonlinelibrary.com]

are generated in regions of high gradients in the velocity field, more viscoelastic stresses would be generated for drops with higher Reynolds number. Hence, with an increase in the viscosity ratio, we observe that the elastic energy in the drop also increases. Since, the drop rises with a higher rise velocity, the position of the drop shall also be higher and we observe the same in Figure 11A. Figure 11B presents the temporal evolution of the diameter of the drop at the axis of symmetry. We can observe that the effects of viscosity ratio is negligible till around $t = 5$. After that, the diameter of the drop decreases more at lower viscosity ratios and the same phenomenon is observed in the sphericity of the drop in Figure 11C.

4.3.2 | Influence of Newtonian solvent ratio on the drop dynamics

To study the influence of Newtonian solvent ratio on the rising drop dynamics, we consider the base case flow parameters and vary only the Newtonian solvent ratio of the drop. We consider the following five different Newtonian solvent ratios in this study: (i) $\beta_1 = 0.5$, (ii) $\beta_1 = 0.625$, (iii) $\beta_1 = 0.75$, (iv) $\beta_1 = 0.875$, and (v) $\beta_1 = 1.0$. The case $\beta_1 = 1.0$, represents a Newtonian drop rising in a Newtonian fluid column. Figure 12 presents the computational results for different Newtonian solvent ratios. Lower the Newtonian solvent ratio, greater is the polymeric viscosity and lesser is the Newtonian viscosity, thereby increasing the viscoelastic character of the drop. Hence with an increase in the viscoelastic character of the drop, it deforms more at the trailing end. In Figure 12A, we can observe that the degree of dimpleness increases with decreasing Newtonian solvent ratio. Thus, the diameter of the drop at the axis of symmetry as well decreases with a decrease in the Newtonian solvent ratio, see Figure 12B. Similar behavior is also observed in the sphericity of the drop. Furthermore, initially the kinetic energy and rise velocity of the drop increases with a decrease in the Newtonian solvent ratio. However, after around $t = 17$, the trend reverses. Figure 12E presents the temporal evolution of the elastic energy in the drop. Till $t = 8.0$, the magnitude of increase in the elastic energy in the drop increases with a decrease in the Newtonian solvent ratio. However, after $t = 8.0$ the trend reverses.

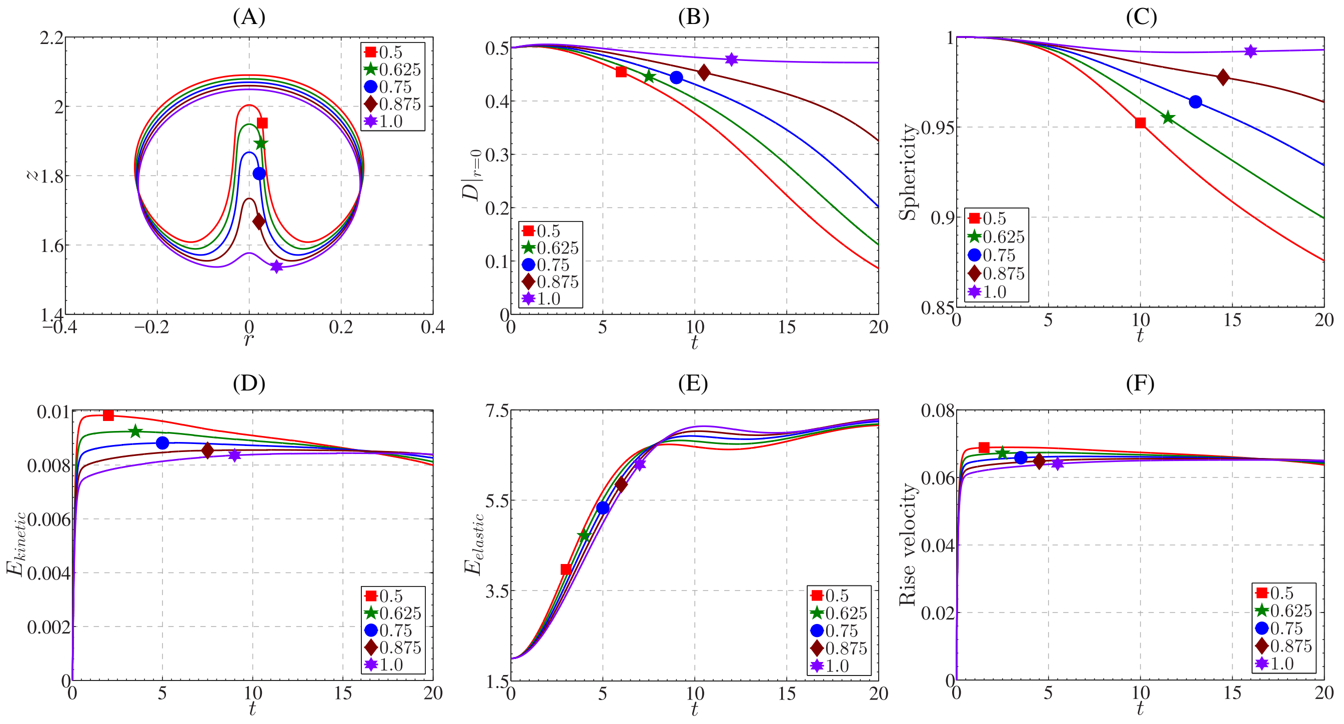

FIGURE 12 Influence of Newtonian solvent ratio for a viscoelastic drop rising in a Newtonian fluid column: (A) drop shape at $t = 20$, (B) diameter of the drop at $r = 0$, (C) sphericity, (D) kinetic energy, (E) elastic energy, and (F) rise velocity of the drop for different Newtonian solvent ratios (i) $\beta_1 = 0.5$, (ii) $\beta_1 = 0.625$, (iii) $\beta_1 = 0.75$, (iv) $\beta_1 = 0.875$, and (v) $\beta_1 = 1.0$ with flow parameters $Re_2 = 10$, $Eo = 400$, $Wi_1 = 10$, $\rho_1/\rho_2 = 0.1$, $\varepsilon = 2$, $\beta_2 = 1.0$, $\alpha_1 = 0.1$, $D = 0.5$, and $h_c = 2.5$ [Color figure can be viewed at wileyonlinelibrary.com]

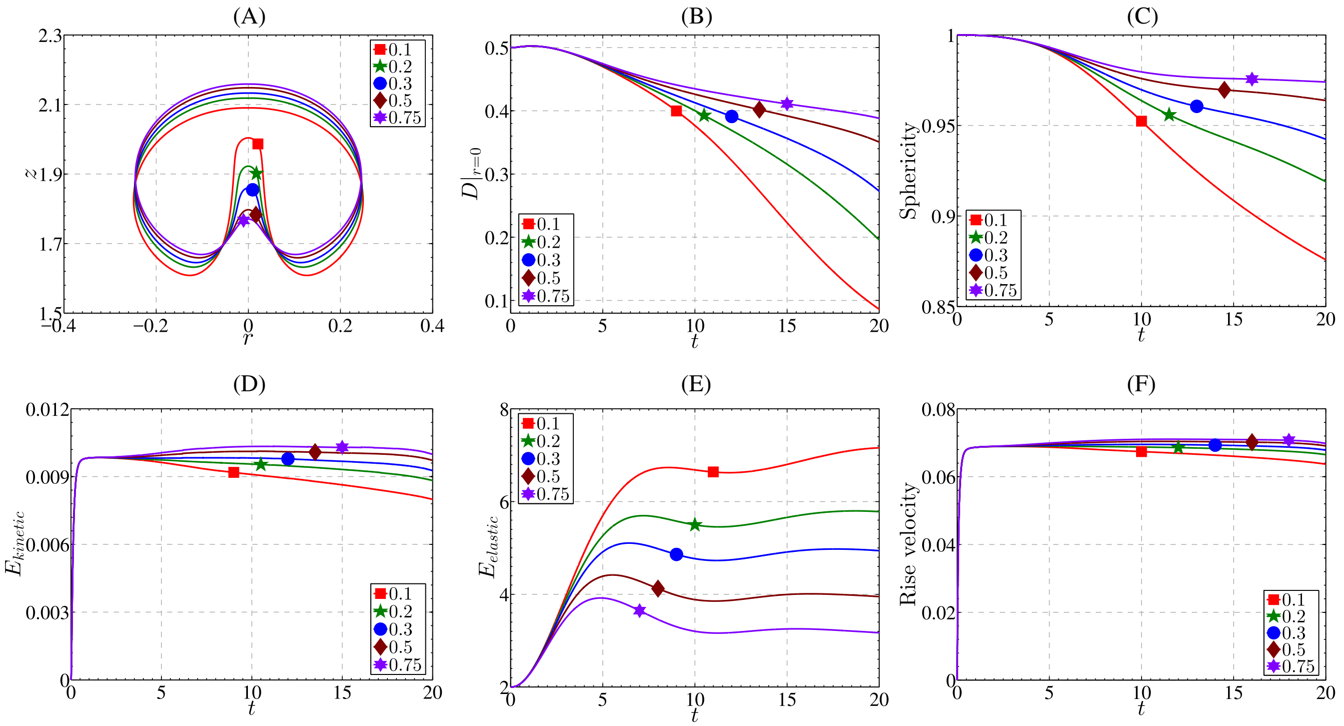

FIGURE 13 Influence of Giesekus mobility factor for a viscoelastic drop rising in a Newtonian fluid column: (A) drop shape at $t = 20$, (B) diameter of the drop at $r = 0$, (C) sphericity, (D) kinetic energy, (E) elastic energy, and (F) rise velocity of the drop for different Giesekus factors (i) $\alpha_1 = 0.1$, (ii) $\alpha_1 = 0.2$, (iii) $\alpha_1 = 0.3$, (iv) $\alpha_1 = 0.5$, and (v) $\alpha_1 = 0.75$ with flow parameters $\mathrm{Re}_2 = 10$, $\mathrm{Eo} = 400$, $\mathrm{Wi}_1 = 10$, $\rho_1/\rho_2 = 0.1$, $\varepsilon = 2$, $\beta_1 = 0.5$, $\beta_2 = 1.0$, $D = 0.5$, and $h_c = 2.5$ [Color figure can be viewed at wileyonlinelibrary.com]

4.3.3 | Influence of Giesekus mobility factor on the drop dynamics

In this section, we study the influence of Giesekus mobility factor on the viscoelastic drop rising in a Newtonian fluid column. We consider the base case flow parameters and use the following five different Giesekus factors: (i) $\alpha_1 = 0.1$, (ii) $\alpha_1 = 0.2$, (iii) $\alpha_1 = 0.3$, (iv) $\alpha_1 = 0.5$, and (v) $\alpha_1 = 0.75$. Figure 13 presents the numerical results for different Giesekus factors. Initially, the motion of the drop is inertia dominated and the Giesekus factor comes into play only when the viscoelastic stresses dominate the flow. Hence, there is no effect of Giesekus factor on the drop dynamics till about $t = 3.0$. However, after that the rise velocity and kinetic energy in the drop increases with an increase in the Giesekus factor, as shear thinning effects increases. Increasing the Giesekus factor leads to a decrease in the magnitude of the viscoelastic stresses generated in the drop. Hence, from Figure 13E we can observe that the magnitude of increase in the elastic energy decreases with an increase in the Giesekus factor. Furthermore, from Figure 13A we can observe that at low Giesekus factor, the effect of dimpleness is higher. Thus, the diameter and sphericity of the drop decreases more with a decrease in the Giesekus factor, refer Figure 13B,C, respectively.

4.3.4 | Influence of Eötvös number on the drop dynamics

In this section, we study the influence of Eötvös number on the rising viscoelastic drop dynamics in a Newtonian fluid column. We consider the base case flow parameters and vary only the Eötvös number, that is, vary the interfacial tension. Six different values are used for the Eötvös number in this study, which are as follows: (i) Eo = 100, (ii) Eo = 175, (iii) Eo = 250, (iv) Eo = 300, (v) Eo = 400, and (vi) Eo = 600. Increasing the Eötvös number, decreases the interfacial tension, thereby making the interface more easily deformable. Thus, from Figure 14A we can observe that at high Eötvös numbers, the drop is more dimpled. In fact at low Eötvös numbers, the drop shapes are more similar to a Newtonian drop rising in a Newtonian fluid column. With further advancement in time, drops with low Eötvös numbers still do not deform as observed with high Eötvös numbers. This is due to the fact that there exists a critical capillary number, beyond

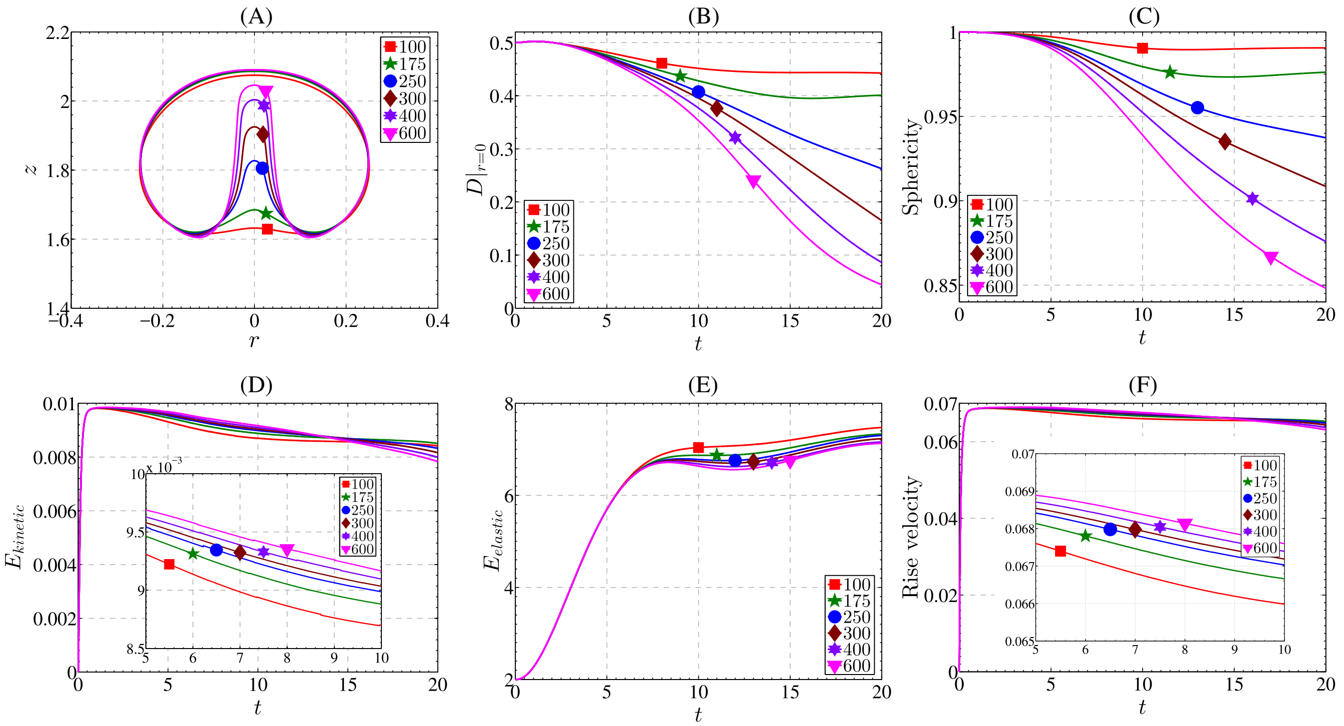

FIGURE 14 Influence of Eötvös number for a viscoelastic drop rising in a Newtonian fluid column: (A) drop shape at $t = 20$, (B) diameter of the drop at $r = 0$, (C) sphericity, (D) kinetic energy, (E) elastic energy, and (F) rise velocity of the drop for different Eötvös numbers (i) Eo = 100, (ii) Eo = 175, (iii) Eo = 250, (iv) Eo = 300, (v) Eo = 400, and (vi) Eo = 600 with flow parameters $\mathrm{Re}_2 = 10$, $\mathrm{Wi}_1 = 10$, $\rho_1/\rho_2 = 0.1$, $\varepsilon = 2$, $\beta_1 = 0.5$, $\beta_2 = 1.0$, $\alpha_1 = 0.1$, $D = 0.5$, and $h_c = 2.5$ [Color figure can be viewed at wileyonlinelibrary.com]

which the drop experiences unsteady deformations in the form of a dimpled shape. From Figure 14A, we can comment that the critical Eötvös number for unsteady drop shapes is between 175 and 250 for the considered flow parameters. Since the trailing end of the drop is pulled more with an increase in the Eötvös number, the diameter of the drop at the axis of symmetry and the sphericity of the drop decreases, see Figure 14B,C, respectively. Furthermore, Figure 14E presents the temporal evolution of the elastic energy in the drop. Till around $t = 6$, there is no effect of Eötvös number on the elastic energy in the drop. However, after that the magnitude of increase in the elastic energy of the drop decreases with an increase in the Eötvös number.

5 | SUMMARY AND OBSERVATIONS

A finite element scheme using the ALE approach is presented for computations of 3D-axisymmetric viscoelastic two-phase flows. The coupled Navier-Stokes and the Giesekus constitutive equations, which describe the viscoelastic flow dynamics is solved monolithically using the proposed numerical scheme. The highlights of the numerical scheme for viscoelastic two-phase flows are the tangential gradient operator technique for the curvature approximation with semiimplicit treatment, ALE approach with moving meshes to track the interface, 3D-axisymmetric variational form using cylindrical coordinates, and the three-field LPS formulation. This stabilized scheme allows to use equal order interpolation for the velocity and the viscoelastic stress, whereas inf-stable finite elements is used for the velocity and the pressure. First-order implicit Euler method is used for the time discretization. Furthermore, the linear elastic mesh update technique is used to displace the inner mesh points of the computational domain and it avoids quick distortion of the mesh.

The numerical scheme is first validated for a 2D planar Newtonian drop rising in a Newtonian fluid column using benchmark results in the literature. Next, a grid independence test is performed for the benchmark configuration to obtain a suitable mesh for grid-independent numerical solutions. A comprehensive numerical investigation is performed for a Newtonian drop rising in a viscoelastic fluid column and a viscoelastic drop rising in a Newtonian fluid column.

The effects of the viscosity ratio, Newtonian solvent ratio, Giesekus mobility factor, and Eötvös number on the rising drop dynamics are analyzed.

The observations are summarized as follows. It is observed that beyond a critical Eötvös number, a Newtonian drop rising in a viscoelastic fluid column experiences an extended trailing edge with a cusp-like shape. For interface flows with high viscosity ratios or low Newtonian solvent ratios or low Giesekus mobility factors or high Eötvös numbers, the effect of viscoelasticity in the bulk fluid column increases leading to an even longer and sharper trailing edge. Furthermore, a negative wake phenomena, where the velocity at the vicinity of the trailing end is in the direction of the drop, but slightly further away from the trailing end the velocity reverses its direction is observed in this study. Next, an indentation around the rear stagnation point with a dimpled shape is observed when a viscoelastic drop rises in a Newtonian fluid column. With low viscosity ratios or low Newtonian solvent ratios or low Giesekus mobility factors or high Eötvös numbers, the effect of viscoelasticity in the drop increases leading to the rear end of the drop being pulled up more.

NOMENCLATURE

α	Giesekus mobility factor
β	Newtonian solvent ratio
Γ_{Axial}	Symmetry of axis
Γ_D	Dirichlet boundary
Γ_F	Interface between two liquids
Γ_N	Neumann boundary
δt	Time-step length
ε	Ratio between total viscosity of outer and inner phases
κ_h	Fluctuation operator
λ	Relaxation time of polymers
μ_0	Total dynamic viscosity
μ_s	Newtonian solvent viscosity
μ_p	Polymeric viscosity
$\boldsymbol{\nu}_D$	Unit outward normal vector on Dirichlet boundary
$\boldsymbol{\nu}_F$	Unit outward normal vector on interface
$\boldsymbol{\nu}_N$	Unit outward normal vector on Neumann boundary
π_h	Global projection operator
π_K	Local projection operator
ρ	Density of fluid
σ	Interfacial tension
$\boldsymbol{\tau}_N$	Unit tangential vector on Neumann boundary
$\boldsymbol{\tau}_p$	Viscoelastic conformation stress
Φ	2D meridian computational domain of Ω
Φ_1	Inner fluid computational domain in 2D
Φ_2	Outer fluid computational domain in 2D
$\partial\Phi$	Boundary of Φ
$\hat{\Phi}$	Reference meridian domain in 2D
$\boldsymbol{\psi}$	Viscoelastic stress space test function
Ψ	Displacement of inner mesh points
Ω	Computational domain in 3D
Ω_0	Initial computational domain in 3D
Ω_1	Inner fluid computational domain in 3D
Ω_2	Outer fluid computational domain in 3D
$\hat{\Omega}$	Reference computational domain in 3D
$\mathcal{T}_h$	Computational mesh
$\mathcal{A}_t$	ALE mappings
$\mathbb{D}$	Deformation tensor
$\mathbb{I}$	Identity tensor
$\mathbb{P}_{\boldsymbol{\nu}_F}$	Projection operator onto the tangential plane of Γ_F

$\mathbb{S}$	Stress tensor in linear elasticity problem
$\mathbb{S}_{\Gamma_F}$	Interface stress tensor
$\mathbb{T}$	Stress tensor of fluid
$\nabla_{\Gamma_{v_F}}$	Interface gradient operator on Γ_F
id	Identity mapping
tr	Trace
Eo	Eötvös number
Fr	Froude number
Re	Reynolds number
We	Weber number
Wi	Weissenberg number
$\hat{b}_{\triangle}$	Cubic polynomial bubble function on the reference triangle
g	Gravitational constant
h_K	Diameter of a cell
h_0	Initial mesh size
p	Pressure
q	Pressure space test function
t	Time
D	Diameter of the drop at symmetry axis
D_h	Discontinuous projection space
E_{elastic}	Elastic energy in the drop
E_{kinetic}	Kinetic energy in the drop
K	Cell
$\hat{K}$	Reference cell
I	Given end time
L	Characteristic length
$\tilde{Q}$	Pressure space in $\Phi(t)$
Q	Pressure space in $\Omega(t)$
$\tilde{S}$	Viscoelastic stress space in $\Phi(t)$
S	Viscoelastic stress space in $\Omega(t)$
U_∞	Characteristic velocity
$\tilde{V}$	Velocity space in $\Phi(t)$
V	Velocity space in $\Omega(t)$
Y_h	Approximation space
$\mathbf{d}$	Displacement of boundary vertices
$\mathbf{e}$	Unit vector in the direction of gravitational force
$\mathbf{u}$	Fluid velocity
$\mathbf{v}$	Velocity space test function
$\mathbf{w}$	Domain velocity
$\mathbf{X}$	Eulerian coordinate
$\mathbf{Y}$	ALE coordinate
$\mathbf{Z}$	Boundary vertices in computational mesh

ORCID

Jagannath Venkatesan https://orcid.org/0000-0001-8892-7270

REFERENCES

1. Liu YJ, Liao TY, Joseph DD. A two-dimensional cusp at the trailing edge of an air bubble rising in a viscoelastic liquid. *J Fluid Mech*. 1995;304:321-342.
2. Sostarecz MC, Belmonte A. Motion and shape of a viscoelastic drop falling through a viscous fluid. *J Fluid Mech*. 2003;497:235-252.
3. Pilz C, Brenn G. On the critical bubble volume at the rise velocity jump discontinuity in viscoelastic liquids. *J Non-Newtonian Fluid Mech*. 2007;145(2–3):124-138.

4. Amirnia S, Bruyn DJR, Bergougnou MA, Margaritis A. Continuous rise velocity of air bubbles in non-Newtonian biopolymer solutions. *Chem Eng Sci*. 2013;94:60-68.
5. Xu X, Zhang J, Liu F, Wang X, Wei W, Liu Z. Rising behavior of single bubble in infinite stagnant non-Newtonian liquids. *Int J Muliphase Flow*. 2017;95:84-90.
6. Izbassarov D, Muradoglu M. A front-tracking method for computational modeling of viscoelastic two-phase flow systems. *J Non-Newtonian Fluid Mech*. 2015;223:122-140.
7. Figueiredo RA, Oishi CM, Afonso AM, Tasso IVM, Cuminato JA. A two-phase solver for complex fluids: studies of the Weissenberg effect. *Int J Multiphase Flow*. 2016;84:98-115.
8. Walters MJ, Phillips TN. A non-singular boundary element method for modelling bubble dynamics in viscoelastic fluids. *J Non-Newtonian Fluid Mech*. 2016;235:109-124.
9. Zainali A, Tofighi N, Shadloo MS, Yildiz M. Numerical investigation of Newtonian and non-Newtonian multiphase flows using ISPH method. *Comput Methods Appl Mech Eng*. 2013;254:99-113.
10. Vahabi M, Kamkari B. Simulating gas bubble shape during its rise in a confined polymeric solution by WC-SPH. *Eur J Mech B Fluids*. 2019;75:1-14.
11. Oldroyd JG. On the formulation of rheological equations of state. *Proc Royal Soc Lond: Ser A*. 1950;200:523-541.
12. Giesekus H. A simple constitutive equation for polymeric fluids based on the concept of deformation-dependent tensorial mobility. *J Non-Newtonian Fluid Mech*. 1982;11:69-109.
13. Bird RB, Dotson PJ, Johnson NL. Polymer solution rheology based on a finitely extensible bead-spring chain model. *J Non-Newtonian Fluid Mech*. 1980;7:213-235.
14. Chilcott MD, Rallison JM. Creeping flow of dilute polymer solutions past cylinders and spheres. *J Non-Newtonian Fluid Mech*. 1988;29:381-432.
15. Thien NP, Tanner RI. A new constitutive equation derived from network theory. *J Non-Newtonian Fluid Mech*. 1977;2:353-365.
16. Verbeeten WMH, Peters GWM, Baaijens FPT. Differential constitutive equations for polymer melts: the extended pom-pom model. *J Rheol*. 2001;45(4):823-843.
17. James AJ, Lowengrub J. A surfactant-conserving volume-of-fluid method for interfacial flows with insoluble surfactant. *J Comput Phys*. 2004;201:685-722.
18. Olsson E, Kreiss G. A conservative level set method for two phase flow. *J Comput Phys*. 2005;210:225-246.
19. Castillo E, Baiges J, Codina R. Approximation of the two-fluid flow problem for viscoelastic fluids using the level set method and pressure enriched finite element shape functions. *J Non-Newtonian Fluid Mech*. 2015;225:37-53.
20. Tryggvason G, Bunner B, Esmaeeli A, et al. A front-tracking method for the computations of multiphase flow. *J Comput Phys*. 2001;169(2):708-759.
21. Yon S, Pozrikidis C. A finite-volume/boundary-element method for flow past interfaces in the presence of surfactants, with application to shear flow past a viscous drop. *Comput Fluids*. 1998;27(8):879-902.
22. Lai MC, Huang C, Huang Y. Simulating the axisymmetric interfacial flows with insoluble surfactant by immersed boundary method. *Int J Numer Anal Model*. 2011;8(1):105-117.
23. Teigen KE, Song P, Lowengrub J, Vogit A. A diffuse-interface method for two-phase flows with soluble surfactants. *J Comput Phys*. 2011;230:375-393.
24. Ganesan S, Tobiska L. An accurate finite element scheme with moving meshes for computing 3D-axisymmetric interface flows. *Int J Numer Methods Fluids*. 2008;57(2):119-138.
25. Codina R, Houzeaux G, Coppola-Owen H, Baiges J. The fixed-mesh ALE approach for the numerical approximation of flows in moving domains. *J Comput Phys*. 2009;228:1591-1611.
26. Baiges J, Codina R, Pont A, Castillo E. An adaptive fixed-mesh ALE method for free surface flows. *Comput Methods Appl Mech Eng*. 2017;313:159-188.
27. Pillapakkam SB, Singh P. A level-set method for computing solutions to viscoelastic two-phase flow. *J Comput Phys*. 2001;174:552-578.
28. Pillapakkam SB, Singh P, Blackmore D, Aubry N. Transient and steady state of a rising bubble in a viscoelastic fluid. *J Fluid Mech*. 2007;589:215-252.
29. Chinyoka T, Renardy YY, Renardy M, Khismatullin DB. Two-dimensional study of drop deformation under simple shear for Oldroyd-B liquids. *J Non-Newtonian Fluid Mech*. 2005;130:45-56.
30. Habla F, Marschall H, Hinrichsen O, Dietsche L, Jasak H, Favero JL. Numerical simulation of viscoelastic two-phase flows using openFOAM. *Chem Eng Sci*. 2011;66:5487-5496.
31. Harvie DJE, Cooper-White JJ, Davidson MR. Deformation of a viscoelastic droplet passing through a microfluidic contraction. *J Non-Newtonian Fluid Mech*. 2008;155:67-79.
32. Yue P, Feng JJ, Liu C, Shen J. Diffuse-interface simulations of drop coalescence and retraction in viscoelastic fluids. *J Non-Newtonian Fluid Mech*. 2005;129:163-176.
33. Yue P, Zhou C, Feng JJ, Ollivier-Gooch CF, Hu HH. Phase-field simulations of interfacial dynamics in viscoelastic fluids using finite elements with adaptive meshing. *J Comput Phys*. 2006;219:47-67.
34. Zhang Y, Wang H, Tang T. Simulating two-phase viscoelastic flows using moving finite element methods. *Commun Comput Phys*. 2010;7(2):333-349.
35. You R, Borhan A, Haj-Hariri H. A finite volume formulation for simulating drop motion in a viscoelastic two-phase system. *J Non-Newtonian Fluid Mech*. 2008;153:109-129.

36. You R, Haj-Hariri H, Borhan A. Confined drop motion in viscoelastic two-phase systems. *Phys Fluids*. 2009;21:013102.
37. Chung C, Hulsen MA, Kim JM, Ahn KH, Lee SJ. Numerical study on the effect of viscoelasticity on drop deformation in simple shear and 5:1:5 planar contraction/expansion microchannel. *J Non-Newtonian Fluid Mech*. 2008;155:80-93.
38. Chung C, Kim JM, Hulsen MA, Ahn KH, Lee SJ. Effect of viscoelasticity on drop dynamics in 5:1:5 contraction/expansion microchannel flow. *Chem Eng Sci*. 2009;64:4515-4524.
39. Mukherjee S, Sarkar K. Effects of viscoelasticity on the retraction of a sheared drop. *J Non-Newtonian Fluid Mech*. 2010;165:340-349.
40. Mukherjee S, Sarkar K. Viscoelastic drop falling through a viscous medium. *Phys Fluids*. 2011;23:013101.
41. Lind SJ, Phillips TN. The effect of viscoelasticity on a rising gas bubble. *J Non-Newtonian Fluid Mech*. 2010;165:852-865.
42. Izbassarov D, Muradoglu M. A computational study of two-phase viscoelastic systems in a capillary tube with a sudden contraction/expansion. *Phys Fluids*. 2016;28:012110.
43. Ganesan S, Matthies G, Tobiska L. On spurious velocities in incompressible flow problems with interfaces. *Comput Methods Appl Mech Eng*. 2007;196(7):1193-1202.
44. Ganesan S. Simulations of impinging droplets with surfactant-dependent dynamic contact angle. *J Comput Phys*. 2015;301:178-200.
45. Venkatesan J, Ganesan S. Computational modeling of impinging viscoelastic droplets. *J Non-Newtonian Fluid Mech*. 2019;263:42-60.
46. Brooks AN, Hughes TJR. Streamline upwind/Petrov-Galerkin formulations for convection dominated flows with particular emphasis on the incompressible Navier-Stokes equations. *Comput Methods Appl Mech Eng*. 1982;32:199-259.
47. Guenette R, Fortin M. A new mixed finite element method for computing viscoelastic flows. *J Non-Newtonian Fluid Mech*. 1995;60:27-52.
48. Fortin A, Guenette R, Pierre R. On the discrete EVSS method. *Comput Methods Appl Mech Eng*. 2000;189(1):121-139.
49. Fortin M, Fortin A. A new approach for the FEM simulation of viscoelastic flows. *J Non-Newtonian Fluid Mech*. 1989;32:295-310.
50. Coronado OM, Arora D, Behr M, Pasquali M. Four-field Galerkin/least-squares formulation for viscoelastic fluids. *J Non-Newtonian Fluid Mech*. 2006;140(1–3):132-144.
51. Kwack J, Masud A. A three-field formulation for incompressible viscoelastic fluids. *Int J Eng Sci*. 2010;48(11):1413-1432.
52. Castillo E, Codina R. Variational multi-scale stabilized formulations for the stationary three-field incompressible viscoelastic flow problem. *Comput Methods Appl Mech Eng*. 2014;279:579-605.
53. Fattal R, Kupferman R. Time-dependent simulation of viscoelastic flows at high Weissenberg number using the log-conformation representation. *J Non-Newtonian Fluid Mech*. 2005;126:23-37.
54. Venkatesan J, Ganesan S. A three-field local projection stabilized formulation for computations of Oldroyd-B viscoelastic fluid flows. *J Non-Newtonian Fluid Mech*. 2017;247:90-106.
55. Venkatesan J, Padmanabhan A, Ganesan S. Simulation of viscoelastic two-phase flows with insoluble surfactants. *J Non-Newtonian Fluid Mech*. 2019;267:61-77.
56. Hysing S, Turek S, Kuzmin D, et al. Quantitative benchmark computations of two-dimensional bubble dynamics. *Int J Numer Methods Fluids*. 2009;60:1259-1288.
57. Barrenechea GR, Castillo E, Codina R. Time-dependent semidiscrete analysis of the viscoelastic fluid flow problem using a variational multiscale stabilized formulation. *IMA J Numer Anal*. 2019;39:792-819.
58. Ervin VJ, Miles WW. Approximation of time-dependent viscoelastic fluid flow: SUPG approximation. *SIAM J Numer Anal*. 2003;41:457-486.
59. Shewchuk JR. Triangle: engineering a 2D quality mesh generator and delaunay triangulator. In: Lin MC, Manocha D, eds. *Applied Computational Geometry: Towards Geometric Engineering*. 1148 of Lecture Notes in Computer Science. Berlin, Germany: Springer-Verlag; 1996:203-222 From the First ACM Workshop on Applied Computational Geometry.
60. Shewchuk JR. Delaunay refinement algorithms for triangular mesh generation. *Comput Geom: Theor Appl*. 2002;22(1–3):21-74.
61. Becker R, Braack M. A finite element pressure gradient stabilization for the Navier-Stokes equations based on local projections. *Calcolo*. 2001;38:173-199.
62. Becker R, Braack M. A two-level stabilization scheme for the Navier-Stokes equations. In: Feistauer M, Dolejši V, Knobloch P, Najzar K, eds. *Numerical Mathematics and Advanced Applications*. Berlin Heidelberg: Springer; 2004:123-130.
63. Braack M, Burman E. Local projection stabilization for the Oseen problem and its interpretation as a variational multiscale method. *SIAM J Numer Anal*. 2006;43(6):2544-2566.
64. Matthies G, Skrzypacz P, Tobiska L. A unified convergence analysis for local projection stabilisations applied to the Oseen problem. *ESAIM Math Model Numer Anal*. 2007;41(4):713-742.
65. Ganesan S, Matthies G, Tobiska L. Local projection stabilization of equal order interpolation applied to the Stokes problem. *Math Comput*. 2008;77(264):2039-2060.
66. Ganesan S, Tobiska L. Stabilization by local projection for convection-diffusion and incompressible flow problems. *J Sci Comput*. 2010;43(3):326-342.
67. John V, Knobloch P, Savescu SB. A posteriori optimization of parameters in stabilized methods for convection-diffusion problems - Part I. *Comput Methods Appl Mech Eng*. 2011;200:2916-2929.
68. Bänsch E. Finite element discretization of the Navier-Stokes equations with a free capillary surface. *Numer Math*. 2001;88:203-235.
69. Amestoy PR, Duff IS, L'Excellent JY, Koster J. A fully asynchronous multifrontal solver using distributed dynamic scheduling. *SIAM J Matrix Anal Appl*. 2001;23(1):15-41.
70. Amestoy PR, Guermouche A, L'Excellent JY, Pralet S. Hybrid scheduling for the parallel solution of linear systems. *Parallel Comput*. 2006;32(2):136-156.

71. Wilbrandt U, Bartsch C, Ahmed N, et al. ParMooN: a modernized program package based on mapped finite elements. *Comput Math Appl*. 2017;74(1):74-88.
72. Hassager O. Negative wake behind bubbles in non-Newtonian liquids. *Nature*. 1979;279:402-403.

SUPPORTING INFORMATION

Additional supporting information may be found online in the Supporting Information section at the end of this article.

How to cite this article: Venkatesan J, Ganesan S. Finite element computations of viscoelastic two-phase flows using local projection stabilization. *Int J Numer Meth Fluids*. 2020;1–30. https://doi.org/10.1002/fld.4808